Maturation of Hippocampus-Medial Prefrontal Cortex Projections Defines a Pathway-Specific Sensitive Period for Cognitive Flexibility

Arely Cruz-Sanchez[1,2], Kathleen E. LaDouceur[1], Anusha Abdusalom[1], Helen Chasiotis[1], Radu Gugustea[1], Mehreen Inayat[1], Unza Mumtaz[1], Maryam Hasantash[3], Christoph Anacker[3] and Maithe Arruda-Carvalho[1,2†]

[1] University of Toronto Scarborough, Department of Psychology, Toronto, Ontario, Canada, M1C1A4

[2] University of Toronto Scarborough, Department of Cell and Systems Biology, Toronto, Ontario, Canada, M1C1A4

[3]Department of Psychiatry, Columbia University, and Research Foundation for Mental Hygiene, Inc. (RFMH), New York State Psychiatric Institute (NYSPI), New York, NY, 10032, USA

[†]Correspondence should be addressed to:

Maithe Arruda-Carvalho
University of Toronto Scarborough, Department of Psychology
1265 Military Trail, Science Wing, Room SW533, Toronto, ON, M1C 1A4, Canada
m.arrudacarvalho@utoronto.ca
@arrudacarvalho.bsky.social

Summary (150 words)

The septotemporal axis of the hippocampus separates it into domains with unique molecular, cellular, downstream connectivity and behavioral profiles, and yet very little is known about the ontogenesis of these highly specialized subcircuits. Here, we used viral tracing, optogenetic-assisted patch clamping, chemogenetics and behavior in mice to examine changes in domain-defined hippocampus efferent projections from postnatal day (P)10 to P60. We found distinct anatomical and synaptic developmental signatures in ventral and intermediate CA1 downstream connectivity, with unique contributions to the prelimbic and infralimbic subregions of the medial prefrontal cortex (mPFC). Juvenile inhibition of the ventral and intermediate CA1-mPFC pathways led to opposing modulation of adult cognitive flexibility, establishing a sex- and pathway-specific sensitive period preceding the stabilization of CA1-mPFC synaptic transmission. Our data elucidate domain- and target-defined postnatal maturation of hippocampus efferents, identifying juvenility as a CA1-mPFC sensitive period with crucial implications for early life influences on adult cognition.

Keywords: Ventral CA1, intermediate CA1, electrophysiology, mice, cognitive flexibility, set shifting, optogenetics, chemogenetics.

Acknowledgements: This work was supported by a Natural Science and Engineering Council of Canada (NSERC) CGS-D (CGSD3 - 534884 – 2019) for AC-S, a grant from the NIH (R01MH126105) to CA, as well as grants from the Natural Science and Engineering Council of Canada (RGPIN-2017-06344), SickKids Foundation and Canadian Institutes of Health Research (CIHR) – Institute of Human Development, Child and Youth Health (NI19-1132R), CIHR (PJT 399790), and Human Frontier

Science Program Organization (CDA00009/2018 and RGY0072/2019) to MA-C. We acknowledge resources and support from the Centre for the Neurobiology of Stress (CNS) Core Facility at the University of Toronto Scarborough, and thank Durga Acharya and Bruno Chue for their help in the facility. A Canada Foundation for Innovation grant (#493864) was used to establish the Centre for the Neurobiology of Stress (CNS) Core Facility.

Author contributions: AC-S, KEL, AA, HC, RG, MI and UM performed research. AC-S, KEL, AA, HC, MI and MA-C analyzed data. MH and CA contributed to study design, data interpretation and writing of the paper. AC-S, KEL and MA-C designed research and wrote the paper.

Declaration of interests: The authors declare no competing interests.

Supplemental information:
Document S1: Figures S1–S8, Supplemental Table S1

Introduction

The hippocampus (HPC) plays a key role in learning and memory[1,2], anxiety-like behavior[3–5] and stress[6], with substantial evidence of distinct downstream pathway-specific contributions to these behaviors. Hippocampal projections to the lateral septum (LS) and basolateral amygdala (BLA) underlie fear memory processing and motivated behavior[7–9], while projections to the thalamic nucleus reuniens (Re) and medial prefrontal cortex (mPFC) are involved in working spatial memory and episodic memory[10–12]. Hippocampal projections to the nucleus accumbens (NAc) and lateral hypothalamus (LH) have been linked to anxiety, social interaction and feeding behavior[9,13]. HPC topographical organization across the septotemporal axis[14–16]

77 distinguishes three HPC domains: dorsal, intermediate and ventral HPC, which diverge
78 in their cellular composition[17–21], efferent/afferent projection patterns[6,22,23], population
79 encoding[24,25] and behavioral output[14,26–30]. This HPC tripartite differentiation is present
80 from birth at both the gene expression and topographical afferent pattern levels[31,32], but
81 very little is known about how the postnatal maturation of the HPC and its downstream
82 projections diverge across its domains.

83 Early life is also the time of peak onset for neurodevelopmental and psychiatric
84 disorders[33–35], which often feature deficits in the HPC and mPFC[36–43] and HPC-mPFC
85 connectivity[44–48] in patients and animal models[38–40,44–53]. The HPC-mPFC pathway
86 comprises unidirectional projections from the HPC intermediate and ventral domains to
87 the mPFC[54–58], and supports decision making, reward learning, fear, and anxiety-like
88 behaviors[11,33,59–61], all of which are (i) developmentally regulated[18,38] and (ii) implicated
89 in neurodevelopmental and psychiatric disorders[33,62–64]. Furthermore, similar to the
90 sensory cortex[65–68], both HPC[69–71] and mPFC[51,72–76] display heightened synaptic
91 plasticity and behavioral features in early life consistent with critical periods, which may
92 inform sensitivity to external influences such as stress[66,77–81,74]. Despite this
93 convergence of factors in early life, it is unclear exactly how HPC-mPFC maturation
94 may affect adult behavior and/or risk of neurodevelopmental and mental disorders.

95 Cognitive flexibility, or the ability to adjust behavior in response to changing
96 conditions[82], is an essential facet of adaptive behaviour necessary for survival. Studies
97 in humans broadly implicate the prefrontal cortex in cognitive flexibility[82–84], particularly
98 in the case of extra-dimensional (ED) set shifting[85–87], a finding replicated in
99 primates[88,89] and rodents[90–93]. Importantly, HPC lesions also feature deficits in ED set

100 shifting in humans[87]. In rodents, developmental manipulations of ventral HPC impair ED
101 set shifting[94,95] and alter mPFC morphology[95], implicating the HPC-mPFC pathway in
102 ED set shifting. While this is consistent with other research tying HPC-PFC alterations
103 to cognitive flexibility deficits in schizophrenia[96,97], the precise contribution of HPC-
104 mPFC pathways to higher-order cognitive flexibility remains unclear.

105 Despite important contributions to our understanding of HPC-mPFC oscillatory activity
106 in neonatal to juvenile mice[46,55,98,99], and changes in vHPC-mPFC plasticity from
107 adolescence to adulthood[100], a comprehensive survey of the postnatal development of
108 HPC-mPFC synaptic connectivity, and how this developmental trajectory may affect
109 adult cognitive function, is currently missing. To address this gap, we first compared the
110 developmental profile of intermediate and ventral CA1 innervation to brain regions
111 implicated in learning and memory (lateral septum (LS), basolateral amygdala (BLA),
112 mPFC, thalamic nucleus reuniens (Re)), social, anxiety- and depression-like behavior
113 (bed nucleus of the stria terminalis (BNST), lateral hypothalamus (LH), nucleus
114 accumbens (NAc)). We then resolved the synaptic maturation of projections from
115 ventral and intermediate CA1 to either prelimbic or infralimbic layer 5 mPFC pyramidal
116 neurons using optogenetics-assisted patch clamping at postnatal day (P)10, P15, P21,
117 P30 and P60. Finally, we examined the functional implications of these developmental
118 changes by chronically inhibiting the vCA1- or iCA1-mPFC pathways during either
119 juvenility (P15-P30) or adulthood (P60-P75) and testing animals a month later in a
120 cognitive flexibility task. We found that juvenile inhibition of the vCA1-mPFC pathway
121 led to a sex-specific deficit in ED set shifting which was not present when the same
122 inhibition took place in adulthood. Surprisingly, juvenile (but not adult) inhibition of the

123 iCA1-mPFC pathway improved adult ED set shifting in both sexes. Together, these data
124 establish a timeline for the maturation of the HPC-mPFC pathway, highlighting
125 septotemporal differences and target-defined asynchronies in anatomical and synaptic
126 maturation guiding sensitivity to circuit disruption.

127 **Results**

128 ***Dorsal, intermediate and ventral CA1 neurons differ in their projection patterns in***
129 ***adult animals***

130 To understand the developmental timeline of HPC efferent pathway innervation, we first
131 compared the axonal terminal patterns of CA1 neurons from the dorsal, intermediate
132 and ventral HPC domains in adult mice. For consistency with subsequent analyses, we
133 infused the dCA1, iCA1 and vCA1 of P53 C57BL/6J mice with AAV1-ChR2-EYFP virus
134 and processed the brains one week later for histology (Fig. S1A), an interval previously
135 established by our group as sufficient for terminal transport[101]. Target regions were
136 chosen based on their involvement in the regulation of memory and emotional behavior:
137 NAc[102–104], LH[4], LS[105], BNST[106], BLA[4,107], Re[108] and mPFC[109–111]. Consistent with
138 previous reports[14,15,23,112–115], we saw domain-specific differences in CA1 efferent
139 innervation, particularly between dorsal and intermediate/ventral CA1 projections (Fig.
140 S1). We found strong projections from iCA1 and vCA1 to mPFC (Fig. 1SB), NAc core
141 and shell (Fig. S1C), LS (Fig. S1D), BLA (Fig. S1E), LH (Fig. S1F) and Re (Fig. S1G)
142 which were mostly absent in dCA1-infused brains. We noticed strong projections from
143 vCA1 to the BNST (Fig. S1H), which were far weaker for iCA1 and absent for dCA1, as
144 described in the literature[116]. While all HPC domains send projections to the LS (Fig.

145 S1D), the pattern of LS innervations differs between dorsal and intermediate/ventral
146 projections, with the former predominantly innervating dorsomedial LS, and the latter
147 the ventromedial LS (Fig. S1D), as previously reported[117]. We then examined the
148 mPFC, with a focus on its prelimbic (PL) and infralimbic (IL) subregions, given their
149 contributions to memory and cognitive functions[12,30,96,118–122]. We saw strong projections
150 from both iCA1 and vCA1 spanning PL and IL, with the strongest signal in IL and PL
151 layer 6 (Fig. S1B). dCA1 axons in both PL and IL were only visible upon GFP signal
152 amplification using immunofluorescence (Fig. S1B, left). Accordingly, we were unable to
153 evoke terminal signals from this pathway when patching from either PL or IL pyramidal
154 neurons, which prevented us from pursuing experiments exploring the synaptic
155 maturation of dCA1-mPFC projections.
156

157 ***Anatomical maturation of vCA1 and iCA1 projections across the lifespan***

158 Given the lack of overlap in the terminal projection patterns from dCA1 compared to
159 iCA1 and vCA1, we focused our efforts on comparing the maturation of iCA1 and vCA1
160 projections from infancy to adulthood. As ventral and intermediate CA1 projections
161 overlap across most targets tested, we wanted to assess whether these subprojections
162 would show equivalent maturation profiles, at both the anatomical and synaptic levels.
163 First, we quantified CA1 targeting across ages to ensure robust viral transduction
164 across ages and subprojections. Mice were injected with AAV1-ChR2-EYFP virus in
165 either vCA1 or iCA1 and brains were processed for histology one week later at P10,
166 P15, P21, P30 and P60 (Fig. 1A), corresponding to infancy, juvenility, late juvenility,
167 adolescence and adulthood, respectively[123]. We observed that in mice younger than

168 P15, vCA1 is very limited in total area compared to later ages, which precluded robust
169 targeting of vCA1 (but not iCA1) at P10 without spread to CA3 and neighboring areas.
170 Quantification of vCA1 infection area from P15 to P60 showed that the proportion of
171 infected vCA1 area (i.e., ratio of vCA1 EYFP volume and total vCA1 volume) was
172 equivalent across ages (Fig. 1B-C). The volume of infected vCA1 at P15 was lower than
173 all older ages (Fig. 1D, green; one-way ANOVA p=0.0056; post hoc p<0.) to
174 compensate for hippocampal growth during this period (Fig. 1D, grey; one-way ANOVA,
175 p=0.00010; post hoc p< 0.013). There were no differences in vCA1 EYFP intensity (Fig.
176 1E) or sex differences in vCA1 volume across ages (Table S1).

177 Quantification of iCA1 infection showed a higher percentage of iCA1 targeted at P10,
178 but not among other age groups (Fig. 1F-G; one-way ANOVA p=0.00010; post hoc
179 p<0.036). This was likely driven by the significantly smaller volume of iCA1 at P10 (Fig.
180 1H, grey; one-way ANOVA p<0.00010; post hoc p<0.0022), despite a smaller iCA1
181 infected area at P10 compared to older ages (Fig. 1H, green; one-way ANOVA p=0.016;
182 post hoc p<0.047). We found no age-dependent differences in EYFP iCA1 intensity
183 (Fig. 1I) or sex differences in iCA1 volume across ages (Table S1).
184

185 *vCA1 and iCA1 terminals reach target regions by P10*

186 We next examined the age at which CA1 projections arrive to their target regions. vCA1
187 and iCA1 terminals were already present in all target regions by the earliest age tested
188 of P10 (Fig. S2). To determine at what precise age CA1 axon terminals arrive at the
189 mPFC, we infused RetroBeads into the mPFC and examined their transport to CA1 in
190 infant and adult mice (Fig. S3A). We first confirmed that a 5-day incubation period was

191 sufficient for retrograde transport from mPFC to CA1 in adult (8 weeks of age) mice
192 (Fig. S3B). CA1 soma signal was present exclusively at the posterior/temporal HPC, at
193 both the vCA1 and iCA1, but not at the anterior/septal (dorsal) HPC (Fig. S3B). We
194 found soma signal in the CA1 of P10 brains following this same injection interval (Fig.
195 S3C), consistent with our anterograde data (Fig. S2). We then tested the presence of
196 CA1-mPFC projections at the earlier age of P5. There was no soma signal at the HPC
197 of P5 brains (Fig. S3D), suggesting that CA1 axons are absent in the mPFC
198 immediately after birth. As it is unclear how long RetroBeads can remain at a given
199 target site without being uptaken by existing projections, these data conservatively
200 suggest that CA1 axons arrive at the mPFC sometime between P0 and P10 in
201 C57BL/6J mice.
202
203 *Distinct target-defined maturation signatures in vCA1 and iCA1 terminal density*

204 To characterize CA1 terminal density changes across ages, we quantified CA1 axon
205 terminal fluorescent intensity in the NAc, LS, BLA, LH, Re, BNST and mPFC (PL and IL)
206 (Fig. 2A-I; Fig. S4). vCA1 terminal density showed different maturation patterns among
207 LS nuclei (Fig. 2A-C), showing no change in LSD (Fig. 2A; Fig. S4A) and LSI (Fig. 2C;
208 Fig. S4A), but a higher density at P15 compared to P30 and P60 in the LSV (Fig. 2B;
209 one-way ANOVA $p=0.010$; post hoc $p=0.010$; $p=0.030$, respectively). vCA1 terminal
210 density remained stable across ages in the NAc (Fig. 2D-E; Fig. S4B). vCA1 terminal
211 density in the BLA was higher at P15 and P60 compared to P21 (Fig. 2F; one-way
212 ANOVA $p=0.017$; post hoc $p<0.036$; Fig. S4C), but remained stable in the Re (Fig. 2G;
213 Fig. S4D). Interestingly, vCA1 terminal density in both BNST and LH showed a

214 decrease between P15 and P21-30 (Fig. 2H-I; BNST: one-way ANOVA p= 0.0095; post
215 hoc p= 0.044, p= 0.0077 respectively; LH: one-way ANOVA p=0.0068; post hoc p<0.05;
216 Fig. S4E-F). We saw no sex differences in any of the regions examined (Table S1).
217 These data suggest target-defined developmental changes in vCA1 efferent anatomical
218 connectivity, with vCA1 terminal density in regions such as LSD, LSI, NAC and Re
219 remaining stable from P15, while terminals in LSV, BLA, BNST and LH undergo further
220 refinement across ages, emphasized by higher vCA1 terminal density at P15 in most of
221 these regions.

222 We next conducted a similar analysis targeting the iCA1 (Fig. 2J-Q; Fig. S5). iCA1
223 terminal intensity in the LSD and LSI decreased with age, starting at P21 and ending at
224 P30 in the LSD (Fig. 2J: one-way ANOVA p=0.0015; post hoc p<0.031; Fig. S5A), and
225 at P21 in the LSI (Fig. 2K: one-way ANOVA p=0.0010; post hoc p<0.025; Fig. S5A).
226 There were no iCA1 terminals in the LSV (Fig. S1D), indicating that vCA1 is the only
227 source of LSV innervation across the CA1 septotemporal axis. Consistent with our
228 results in the vCA1, iCA1 terminal intensity remained stable across ages in the NAc
229 core (Fig. 2L; Fig. S5B), but increased between P21 and P30 in the NAc shell (Fig. 2M;
230 one-way ANOVA p=0.010; post hoc p=0.0051; Fig. S5B). In further contrast to our vCA1
231 findings, there were no age-dependent changes in iCA1 terminal density in the BLA
232 (Fig. 2N; Fig. S5C), and a surprising dip in iCA1 terminal density at P21 in the Re
233 compared to P30-60 (Fig. 2O; one-way ANOVA p=0.0019; post hoc p<0.010; Fig. S5D)
234 There was no change in iCA1 terminal density in the BNST (Fig. 2P; Fig. S5E), but an
235 increase in the LH starting at P30 and continuing to P60 (Fig. 2Q one-way ANOVA
236 p<0.00010; post hoc p<0.020; Fig. S5F). We found no sex differences in the regions

237 analyzed (Table S1). These data emphasize a distinct pattern of terminal maturation
238 between vCA1 and iCA1 projections, with regions that are predominantly stable across
239 ages in one pathway (e.g., LSD, LSI, NAc shell and Re for vCA1) showing age-
240 dependent changes in terminal density in the other pathway (e.g., iCA1), and vice-
241 versa. A graphical summary of these findings is available in Fig. S6. Together, these
242 data highlight domain- and target-specific time signatures of anatomical connectivity
243 among HPC efferents.

244 We next quantified ventral and intermediate CA1 terminal density in the mPFC, focusing
245 on PL and IL layers 2/3, 5 and 6 (Fig. 3A, H). We saw no differences in vCA1 terminal
246 density from P15 to P60 in PL layers 2/3 (Fig. 3B), 5 (Fig. 3C) or 6 (Fig. 3D), nor across
247 any layers in the IL (Fig. 3E-G). However, P15 females showed increased terminal
248 density in PL and IL layer 6 compared to P15 males (PL: two-way ANOVA $p=0.047$;
249 post hoc $p=0.025$; IL: two-way ANOVA $p=0.037$; post hoc $p=0.039$;Table S1). In
250 contrast to the refinements seen in other vCA1 target regions, anatomical connectivity
251 between vCA1 and the PL/IL remains stable from P15 onwards, with some differences
252 between sexes.

253 When we extended this analysis to iCA1 terminals (Fig. 3H-N), we found significant
254 age-dependent increases in iCA1 terminals in all PL layers starting at P30 (Fig. 3I-K;
255 Layer 2/3: one-way ANOVA $p=0.00090$; post hoc $p<0.0020$; layer 5: one-way ANOVA
256 $p<0.00010$; post hoc $p<0.010$; layer 6: one-way ANOVA $p<0.00010$; post hoc $p<0.050$).
257 These changes were not seen in IL (Fig. 3L-N). There were no sex differences in these
258 datasets (Table S1). These data suggest asynchrony in the anatomical maturation of
259 iCA1 terminals within the mPFC, with a delay in the stabilization of iCA1 innervation of

260 PL relative to the IL, starting at adolescence. Furthermore, these divergent maturation
261 trajectories point to significant septotemporal specialization in the anatomical maturation
262 of iCA1 and vCA1 projections to mPFC, whereby only iCA1 projections to PL display
263 age-dependent changes between infancy and adulthood.
264
265 ***Maturation of CA1-PFC synaptic transmission***

266 Dysfunction in the communication between the intermediate/ventral HPC and the mPFC
267 is a prominent feature of cognitive deficits in rodent models of neurodevelopmental
268 disorders[47], and yet very little is known about the developmental trajectory of synaptic
269 connectivity within this pathway[46,55,98,124]. To address this gap, we focused our
270 investigation on the domain-specific synaptic maturation of CA1-mPFC pathways in
271 C57BL/6J mice.
272
273 *Maturation of spontaneous transmission in PL and IL layer 5 pyramidal neurons*

274 To understand the context in which CA1 axons arrive and influence synaptic
275 transmission in the mPFC, we first investigated the maturation of spontaneous
276 excitatory and inhibitory synaptic transmission in layer 5 PL and IL pyramidal neurons at
277 P10, P15, P21, P30 and P60. Starting with the PL, we saw an increase in the amplitude
278 of spontaneous excitatory postsynaptic currents (sEPSCs) between P10-P21 to P30-
279 P60 (Fig. 4A-B; one-way ANOVA $p<0.00010$; post hoc $p<0.014$), but no change in
280 sEPSC frequency (Fig. 4C) or tau decay time (Fig. 4D). When examining PL
281 spontaneous inhibition, we found a similar increase in the amplitude of spontaneous
282 inhibitory postsynaptic currents (sIPSCs) between P10-21 and P30-P60 (Fig. 4E: one-

283 way ANOVA p<0.00010; post hoc p<0.046) and an earlier increase in sIPSC frequency
284 starting at P21 (Fig. 4F; one-way ANOVA p <0.00010; post hoc p<0.031), but no change
285 in sIPSC decay time (Fig. 4G). A within-cell comparison of sEPSC and sIPSC PL
286 frequencies showed a shift toward increased relative sIPSC frequency at P30 and P60
287 (Fig. 4H; paired t-test p<0.019), which is replicated in the increase in the spontaneous I-
288 E frequency difference at P30 and P60 (Fig. 4I; one-way ANOVA p=0.0020; post hoc
289 p<0.035). We saw sex differences in PL sEPSC and sIPSC amplitude (higher in P30
290 females and P60 males), sEPSC frequency (higher in males at P21 and P30) and
291 sIPSC frequency (higher in males at P30 and P60), sIPSC tau decay time (higher in
292 P60 females), as well as spontaneous I-E frequency differences, with P21 males and
293 P60 females showing greater differences (Table S1). These data point to significant pre-
294 and postsynaptic changes in spontaneous inhibitory transmission in PL layer 5
295 pyramidal neurons between P15-21 and P30, including a shift toward increased
296 spontaneous inhibition that is likely reflective of maturation of local interneurons[125].

297 Parallel analysis of the maturation of IL layer 5 spontaneous transmission showed no
298 change in sEPSC amplitude (Fig. 4J-K) or tau decay time (Fig. 4M), but a peak in
299 sEPSC frequency at P21 compared to P10 (Fig. 4L; one-way ANOVA p=0.017; post hoc
300 p=0.0084). IL layer 5 pyramidal neurons showed an increase in sIPSC amplitude
301 between P15 and P30 (Fig. 4N; one-way ANOVA p=0.048; post hoc p=0.024), and an
302 increase in sIPSC frequency from P21 (Fig. 4O; one-way ANOVA p=0.00010; post hoc
303 p<0.028). There were no age-dependent changes in sIPSC tau decay time (Fig. 4P).
304 Similar to PL, we saw an increase in the relative frequency of spontaneous inhibition at
305 P30-P60 (Fig. 4Q; paired t-test p<0.013) and increased spontaneous inhibition to

306 excitation differences between P10-21 and P60 (Fig. 4R; one-way ANOVA p=0.0017;
307 post hoc p<0.034), but no sex differences in this dataset (Table S1). These data
308 indicate synchronous changes in spontaneous inhibition between PL and IL layer 5
309 neurons, with distinct maturation timelines for spontaneous excitation between
310 subregions.
311
312 *Asynchrony in the maturation of vCA1-PL and vCA1-IL presynaptic transmission*

313 Next, we wanted to examine the maturation of pathway-specific CA1-mPFC synaptic
314 transmission. To do that, we injected AAV1-ChR2 virus into the ventral CA1 one week
315 prior to recording from layer 5 pyramidal neurons in the PL or IL at P15, P21, P30 and
316 P60 (Fig. 5A). We first examined age-dependent changes in CA1-mPFC *pre*synaptic
317 transmission. To assess glutamate release in vCA1-mPFC synapses, we analyzed
318 EPSCs during paired pulse stimulation, whereby the relative amplitude of the second
319 response is modulated by initial release probability. There was a significant decrease in
320 paired pulse ratios (PPR) of vCA1-PL synapses between P21 and later ages (Fig. 5B;
321 Mixed-effects model: main effect of age p=0.00090, interval x age interaction
322 p<0.00010; post hoc 100ms: p<0.029; 250ms: p<0.028; Fig. 5C; 250ms: one-way
323 ANOVA p=0.00040; post hoc p<0.0035), an effect largely driven by changes in females
324 (two-way ANOVA p=0.036; post hoc p=0.0024). This suggests an increase in vCA1-PL
325 release probability starting at adolescence. vCA1-IL paired pulse ratios were lower at
326 P60 compared to P21 (Fig. 6D5D; Two-way ANOVA: interval x age interaction
327 p=0.0036; post hoc 250ms: p=0.018; 500ms: p=0.0010; Fig. 5E; One-way ANOVA
328 p=0.0022; post hoc p=0.020; no sex differences, Table S1), pointing to distinct

329 presynaptic maturation trajectories for vCA1 projections to these mPFC subregions,
330 with the vCA1-PL pathway showing an earlier profile of presynaptic changes between
331 P21 and P30 in females.
332
333 *Projection-specific timing signatures for vCA1- and iCA1-mPFC presynaptic maturation*

334 We then extended this analysis to iCA1-mPFC synapses. Using an identical
335 experimental setup, we infused the iCA1 of mice with AAV1-ChR2 virus and conducted
336 patch clamp recordings one week later at P10, P15, P21, P30 or P60 (Fig. 5J). There
337 was a significant peak in iCA1-PL paired pulse ratios at P15 compared to P10, P30 and
338 P60 (Fig. 5K; Mixed-effects model: main effect of age $p=0.00050$; post hoc 100ms:
339 $p<0.0067$; 250ms: $p<0.025$; 500ms: $p=0.033$; Fig. 5L; 250ms: one-way ANOVA $p=$
340 0.00020; post hoc $p<0.0079$), suggesting a relative increase in presynaptic efficacy in
341 iCA1-PL synapses from P30. When we examined iCA1-IL synapses, we saw a similar
342 decrease in paired pulse ratio between P15-P21 and P60 (Fig. 5M; Mixed-effects
343 model: main effect of age $p<0.00010$; interval x age interaction $p<0.00010$; post hoc
344 100ms: $p<0.0090$; 250ms: $p<0.024$; 500ms: $p<0.030$; 1000ms: $p<0.012$; Fig. 5N;
345 250ms: One-way ANOVA $p=0.0015$; post hoc $p<0.0091$). These data suggest a slight
346 delay in the refinement of presynaptic release probability in iCA1-IL synapses (at P60)
347 relative to iCA1-PL synapses (P30). There were no sex differences in iCA1-IL paired
348 pulse ratios (Table S1). Together, these results reveal a differential time course for the
349 presynaptic maturation of v/iCA1 projections to mPFC subregions, with earlier
350 maturation of v/iCA1-PL presynaptic efficacy (P30) compared to v/iCA1-IL (P60) (see
351 Fig. S7, left panel for a graphic summary of these data).

352

353 *Delayed maturation of iCA1-mPFC postsynaptic efficacy*

354 We next wanted to assess age-dependent changes in CA1-mPFC evoked *post*synaptic
355 transmission. We recorded AMPAR currents and AMPA:NMDA ratios as a function of
356 developmental age in vCA1- and iCA1-PL and IL synapses using the same
357 experimental design described previously (Fig. 5A, J). We saw no change in the
358 amplitude of AMPAR currents (Fig. 5F) or in AMPA:NMDA ratios (Fig. 5G) in vCA1-PL
359 synapses across ages. In vCA1-IL synapses, there was a significant decrease in
360 AMPAR response amplitude between P15 and P60 (Fig. 5H; one-way ANOVA p=0.048;
361 post hoc p=0.033) but no change in AMPA:NMDA ratios (Fig. 5I; no sex differences,
362 Table S1). Given the lack of changes in vCA1-mPFC postsynaptic maturation, we
363 restricted our iCA1 analysis to P15, P30 and P60 age groups to increase experimental
364 output. While vCA1-mPFC postsynaptic transmission remains largely stable between
365 P15 and P60, iCA1-mPFC postsynaptic maturation undergoes marked refinement
366 across this period. There was no change in the amplitude of AMPAR currents (Fig. 5O),
367 but an increase in AMPA:NMDA ratios between P15 and P30 (Fig. 5P; one-way ANOVA
368 p=0.018; post hoc p=0.019), similar to the timeline of presynaptic changes. Analysis of
369 iCA1-IL synapses showed a decrease in AMPAR current amplitude between P15 and
370 P60 (Fig. 5Q; one-way ANOVA p=0.0048; post hoc p=0.0044) and an increase in
371 AMPA:NMDA ratios between P15 and P30 (Fig. 5R; one-way ANOVA p=0.0070; post
372 hoc p<0.028), indicating synchronous maturation of postsynaptic efficacy (AMPA:NMDA
373 ratios) of iCA1 synapses onto PL and IL subregions, which occurs after the stabilization
374 of vCA1-mPFC postsynaptic transmission (from P15). Females showed larger iCA1-IL

375 AMPAR current amplitude compared to males at P15 (Table S1). Overall, these data
376 show domain-, target-, and synaptic locus-defined time signatures of synaptic
377 maturation within the CA1-mPFC pathway. While the timing of v/iCA1 presynaptic
378 maturation seems to be dependent on their target domain (slightly delayed maturation in
379 IL compared to PL), vCA1 synapses display a dissociation between the timing of pre-
380 and postsynaptic refinement (changes in PPR from P30-60 but stable AMPA:NMDA
381 ratios across ages). Within iCA1 projections, iCA1-IL synapses show a delayed onset of
382 presynaptic changes (P60) compared to postsynaptic changes (P30), but iCA1-PL
383 synapses show synchronous changes in PPR and AMPA:NMDA ratios. A visual
384 summary of the evoked CA1-mPFC synaptic maturation data is featured in Figure S7.
385

386 ***Inhibition of CA1-mPFC pathways during juvenility exert opposing effects on***
387 ***adult cognitive flexibility***

388 We then wanted to probe the functional implications of the CA1-mPFC maturation
389 signatures identified by our anatomical and synaptic analyses. Critical periods in the
390 sensory cortex are marked by structural and synaptic changes[65,67,126–130], suggesting
391 that the timing of CA1-mPFC synaptic changes may signal similar sensitive periods in
392 its dependent behavior. To test this, we used an intersectional viral approach to
393 chemogenetically inhibit either the vCA1- or iCA1-mPFC pathways at select
394 developmental timepoints and assess its effects on a cognitive flexibility behavioral task
395 in adulthood (Fig. 6A). We injected a retrograde AAV virus expressing Cre recombinase
396 into the mPFC and a Cre-dependent inhibitory hM4Di AAV virus into the vCA1 or iCA1
397 to selectively inhibit either the vCA1- or iCA1-mPFC pathways via chronic treatment

398 with the agonist C21, which selectively activates hM4Di receptors[131,132] (Fig. 6A). As our
399 electrophysiological data showed marked changes in vCA1-PL presynaptic transmission
400 between P21 and P30 in females, we first targeted our chronic inhibition to the vCA1-
401 mPFC pathway during the juvenile period (P15-P30) in male and female mice, and
402 compared it to an identical manipulation during adulthood (P60-P75) (Fig. 6A). After
403 30d, we tested the animals in an attentional set shifting task[91] for cognitive flexibility in
404 the absence of C21 (Fig. 6A). In this task, mice learn to dig through two types of
405 bedding for a food reward. During rule acquisition, the food reward is associated with a
406 scent, regardless of bedding type (Fig. 6A). After reaching criterion, animals undergo an
407 extradimensional set shifting test, in which the reward predictor switches to bedding
408 type (Fig. 6A).

409 Mice that underwent vCA1-mPFC inhibition (vCA1 hM4D mice) during juvenility (P15-
410 P30) showed similar rates of rule acquisition of the set shifting task performed
411 compared to control mCherry mice in adulthood (Fig. 6B). However, vCA1 hM4D
412 females showed an impairment in extradimensional set shifting (Fig. 6C; two-way
413 ANOVA effect of virus and sex $p<0.00010$, interaction $p=0.0022$; post hoc $p<0.00010$).
414 Importantly, juvenile-inhibited female and male vCA1 hM4D-injected animals did not
415 differ from mCherry-injected mice in terms of time to first choice (Fig. 6D) or distance
416 travelled (Fig. 6E) during ED set shifting, suggesting that the ED set shifting deficit seen
417 in the vCA1 hM4D females is not driven by changes in exploration or motivation during
418 the task. In the adult inhibition cohort, which took place between P60-P75, male and
419 female vCA1 mCherry and hM4D mice showed similar performance at rule acquisition
420 (Fig. 6F) and in ED set shifting (Fig. 6G-I), indicating that the ED set shifting impairment

421 is specific to vCA1-mPFC pathway disruption during juvenility. Importantly, chronic
422 vCA1-mPFC inhibition in either cohort did not affect performance or exploration in the
423 elevated plus maze (Fig. S8), indicating that changes in anxiety-like behavior are not
424 driving the ED set shifting deficit. These findings identify a sex-specific sensitive period
425 within the vCA1-mPFC pathway during early life that is crucial for cognitive flexibility in
426 adulthood.
427 To test whether the iCA1-mPFC pathway would display a similar developmental
428 sensitivity to disruption, we conducted the same experiment but inhibiting mPFC-
429 projecting iCA1 neurons either from P15-P30, a period in which we saw considerable
430 iCA1-mPFC anatomical (Fig. 3I-K) and pre- and postsynaptic changes (Fig. 5K-R), or
431 from P60-P75 (Fig. 6A), after changes had plateaued. Juvenile inhibition of the iCA1-
432 mPFC pathway did not affect rule acquisition (Fig. 6J), but surprisingly facilitated
433 extradimensional set shifting performance in both male and female mice (Fig. 6K; two-
434 way ANOVA effect of virus $p<0.00010$; post hoc $p<0.0011$). iCA1 hM4D- and mCherry-
435 injected mice showed similar time to first choice (Fig. 6L) and distance travelled (Fig.
436 6M) during ED set shifting. In contrast, adult iCA1-mPFC inhibition did not affect
437 performance at rule acquisition (Fig. 6N) or extradimensional set shifting (Fig. 6O). In
438 this cohort, we found a sex difference in the mCherry groups for latency to first choice,
439 as females took slightly longer than males (Fig. 6P; two-way ANOVA effect of sex
440 $p=0.0046$; post hoc $p=0.012$), but no group differences in distance travelled (Fig. 6Q).
441 Altogether, these data highlight a convergence between pathway- (and sex-) specific
442 synaptic and/or anatomical developmental changes and sensitivity to pathway
443 disruption, consolidating juvenility (P15-P30) as a sensitive period for the influence of

444 vCA1- and iCA1-mPFC pathways on adult cognitive flexibility. Importantly, they also
445 uncovered opposite roles for juvenile inhibition of vCA1 and iCA1-mPFC pathways on
446 adult cognitive function.
447 To investigate the effects of our CA1-mPFC chronic manipulations on mPFC circuit
448 function, we next conducted whole-cell patch clamp recordings of PL layer 5 pyramidal
449 neurons in a separate, behaviorally naïve cohort of animals (Fig. 7A). We used the
450 same experimental design as that of the ED set shifting experiments, but recorded from
451 PL layer 5 pyramidal cells 30d following either juvenile (P15-P30) or adult (P60-P75)
452 inhibition of vCA1- or iCA1-mPFC pathways (Fig. 7A). Juvenile inhibition of the vCA1-
453 mPFC pathway had no effect on PL sEPSC amplitude (Fig. 7B-C), but led to a
454 significant decrease in PL sEPSC frequency (Fig. 7D; two-way ANOVA significant
455 interaction p=0.0051; post hoc p=0.0050) and sIPSC amplitude (Fig. 7E; two-way
456 ANOVA effect of virus p=0.024; post hoc p=0.0074) exclusively in females. Importantly,
457 these changes in PL global synaptic transmission occurred in the same group that
458 showed deficits in ED set shifting behavior (Fig. 6C). Adult inhibition of the vCA1-mPFC
459 pathway had no effect on PL pyramidal cell spontaneous transmission (Fig. 7G-K), with
460 the exception of an increase in sEPSC amplitude in adult vCA1 hM4D males (Fig. 7G-
461 H; two-way ANOVA effect of virus p=0.047; post hoc p=0.018).
462 We next examined the effects of iCA1-mPFC chronic inhibition on adult PL spontaneous
463 transmission. Juvenile inhibition of the iCA1-mPFC pathway did not affect sEPSC
464 amplitude (Fig. 7L-M), but led to an increase in sEPSC frequency in iCA1 hM4D males
465 compared to mCherry controls (Fig. 7N; two-way ANOVA effect of virus p=0.0089; post
466 hoc p=0.0085). There were no changes in sIPSC amplitude (Fig. 7O). Interestingly,

467 iCA1-mPFC juvenile inhibition led to an increase in sIPSC frequency exclusively in
468 females (Fig. 7P; two-way ANOVA effect of virus p=0.047, interaction p=0.037; post hoc
469 p=0.011). Thus, the improved ED set shifting behavior seen in both sexes in the juvenile
470 iCA1-mPFC cohort was accompanied by sex-specific changes in mPFC spontaneous
471 transmission, with males showing changes in spontaneous excitation, and females in
472 spontaneous inhibition. Adult inhibition of the iCA1-mPFC pathway had no effect on PL
473 pyramidal cell spontaneous activity (Fig. 7Q-U). Overall, these data suggest that
474 juvenile inhibition of the vCA1- and iCA1-mPFC pathways leads to disturbances in
475 mPFC global synaptic transmission that may underlie their concurrent impact on adult
476 cognitive flexibility.
477

478 **Discussion**

479 Here we used a combination of viral tracing, optogenetic-assisted patch clamping,
480 chemogenetics and behavior to examine septotemporal differences in HPC efferent
481 projections across the lifespan, and their implications for cognitive function in adulthood.
482 This is to our knowledge the first demonstration of a pathway-specific sensitive period
483 for cognitive function. We found that the timing of anatomical refinement of CA1 axons
484 varied both according to the target region and within the CA1 septotemporal axis. While
485 CA1 projections to IL and NAc core remained stable from P10 to P60, vCA1 and iCA1
486 terminal density displayed distinct timing signatures in the PL, LS, NAc shell, Re, BLA,
487 BNST and LH. Focusing on the synaptic maturation of CA1-mPFC projections, we saw
488 an earlier onset of changes in presynaptic transmission in v/iCA1-PL compared to
489 v/iCA1-IL synapses. Developmental changes in postsynaptic transmission also showed

490 asynchrony among these pathways, with a marked delay within iCA1-PL and -IL
491 synapses compared to vCA1 inputs. Finally, we uncovered a pathway- and sex-specific
492 sensitive period for CA1-mPFC pathways during juvenility, leading to distinct modulation
493 of cognitive flexibility in adulthood. Overall, our data consolidate a blueprint for the
494 maturation of CA1-mPFC projections with crucial implications for behavior and the
495 effects of circuit disturbances and/or other factors influencing circuit output from early
496 life.

497 Our anatomical analysis showed unique timing of developmental signatures in vCA1
498 and iCA1 terminal density in the LS, NAc, BNST, LH, Re, BLA and mPFC. Notably,
499 age-dependent refinements in these target regions were exclusive to one of the CA1-
500 mPFC pathways, with the other pathway remaining stable for that time period. While
501 iCA1 terminal density in LSD and LSI decreased from P21, vCA1 terminal density
502 across these two LS subregions remained stable across ages. In rats, HPC projections
503 shift from medial septum to LS at embryonic and perinatal (P1 and P5) stages[8,133], but
504 less is known about HPC-LS maturation following that period. Interestingly, in contrast
505 to our vCA1 data, subiculum projections to the LS increase in density between P0-P30
506 in the rat[134], suggesting possible species and/or subregion developmental differences.

507 While iCA1 terminal pruning occurs synchronously across LS subregions from P10 to
508 later ages, projections to PL increase in density with age, similar to the LH. In rats, the
509 first 2 to 3 postnatal weeks mark major changes in PL cytoarchitecture and an increase
510 in dendritic arborization[135–137], which may be informed by changes in afferent
511 innervation, including from iCA1. While local expression of DCC/netrin guides pathway-
512 specific anatomical innervation trajectories within mesocortical pathways[138–141], the

513 precise signaling molecules guiding the timing and region-specific differences in CA1
514 anatomical maturation still need to be identified. Furthermore, the consistency of
515 collateral patterns seen among certain adult vCA1 subpopulations[142] may contribute to
516 the synchrony between vCA1 terminal changes reported here. Importantly, our
517 functional manipulation cannot exclude the contribution of these collaterals from mPFC-
518 projecting v/iCA1 neurons to ED set shifting performance. Future work will need to
519 dissect the contribution of v/iCA1 subpopulations exclusively targeting the mPFC from
520 those also projecting to amygdala[113], LS[142] and other regions.

521 Our data on age-dependent changes in spontaneous EPSCs and IPSCs at PL layer 5
522 showed a significant shift towards increased global presynaptic inhibition at P30. Our
523 findings are largely consistent with work by Kroon and colleagues which described an
524 increase in sEPSC and sIPSC frequencies between P13-16 and P26-30 in PL layer
525 5[136]. However, Kroon and colleagues report relatively increased excitatory responses
526 compared to ours[136], with differences in the age of the animals or in mouse
527 strain/vendor possibly contributing to this disparity. Our data showed a significant shift
528 toward PL and IL spontaneous inhibitory activity by P21-30, which is consistent with the
529 timing of maturation of inhibitory interneurons in the mPFC between juvenility and
530 adolescence[143–145]. Given the important role of mPFC inhibitory transmission in
531 juvenility and adolescence to adult function[146], dissecting the relative contributions of
532 select input pathways to mPFC interneurons in early life will be key to elucidating the
533 factors regulating this potential sensitive period.

534 We established that iCA1 and vCA1 axons arrive at the mPFC between P0 and P10 in
535 C57BL/6J mice. This is in line with neonatal studies that report HPC oscillatory influence

536 on the mPFC as early as P7 in rats[55,98,147], as well as synaptic connectivity between
537 v/iHPC and PL by P8-10[147]. Although the physiology of glutamatergic monosynaptic
538 projections from the vCA1 to mPFC is well-known in adult mice[113,148–150], very little was
539 known about synaptic transmission within the CA1-mPFC circuit in early life (but see[147]).
540 Following the initial arrival of CA1 axons, we saw marked pathway- and age-dependent
541 changes in CA1-mPFC evoked synaptic activity. Specifically, the major changes
542 occurring in CA1-PL transmission within the second and third postnatal weeks coincide
543 with a P7-P13 shift from presynaptic depression to facilitation in PL layer 5 pyramidal
544 cells following layer 2/3 stimulation in rats[151], as well as the maturation of mPFC fast
545 spiking interneurons and their increase in connectivity with pyramidal neurons in the
546 second postnatal week[145]. Importantly, this period also comprises major changes in
547 mPFC network oscillatory activity[98,145] and strengthening of HPC-mPFC coupling
548 between P8-10 and P16-24[46]. Moreover, changes in CA1 synaptic composition across
549 this same timeline[152] emphasize the need to understand the contribution of
550 developmental changes in synapse structure to the maturation of synaptic connectivity
551 as reported here. Interestingly, local field recordings showed that high frequency
552 stimulation of the vHPC triggers plasticity in the mPFC in adulthood (from P65-85), but
553 not during early (P30-40) or late (P45-55) adolescence in rats[100], suggesting a potential
554 further delay in the maturation of certain plasticity features within this pathway which
555 could be reflected in our adult chronic inhibition changes in sEPSC amplitude (Fig.7H).

556 Our previous work had shown a distinct temporal profile for the anatomical and synaptic
557 maturation of the mPFC-BLA pathway, which displays a delayed arrival and refinement
558 of axons compared to CA1-mPFC projections, but synchronous evoked synaptic

559 changes around P30[101]. Markedly, iCA1-PL, iCA1-IL and mPFC-BLA pathways display
560 an identical timeline of postnatal maturation of AMPA:NMDA ratios, suggesting that pre-
561 and postsynaptic maturation programs might be differentially expressed across
562 specialized projections. The differential timeline for maturation of PL and IL projections
563 also bears important behavioral implications given the distinct roles of these subregions
564 in emotional and cognitive function[120–122]. Altogether, these analyses point to a high
565 degree of specialization in the developmental profiles across brain pathways, whose
566 guiding principles remain unknown. Given the developmental milestones taking place
567 from juvenility to adolescence, including increased exploration and threat exposure
568 upon leaving the nest[153], as well as the emergence of persistent memory formation[154–
569 159], understanding how these time signatures relate to specialized stimulus processing
570 and behavioral output needs further investigation.

571 We found that the timing of changes in CA1-mPFC synaptic transmission marked a
572 sensitive period in the effects of pathway disruption on cognitive flexibility. For the
573 vCA1-mPFC pathway, this effect was exclusive to females, in line with sex-specific
574 changes in vCA1-PL PPR ratio between juvenility and adolescence, and increased
575 vCA1-PL layer 6 terminal density in P15 females compared to males. While the origin
576 and extent of this sex-specific effect in vCA1-mPFC maturation trajectory and sensitivity
577 remain unclear, these data add to a growing literature showing sex differences in
578 various aspects of HPC and mPFC maturation[160–164], and in early life vulnerability to
579 morphological, electrophysiological and synaptic plasticity changes in both the HPC[165–
580 167] and mPFC[80,168–171]. We note that the sex differences in our dataset were mostly
581 restricted to PL maturation of spontaneous excitation and inhibition, as well as changes

582 in vCA1-PL and iCA1-PL PPR, pointing to mPFC subregion selectivity. Nevertheless, it
583 is important to acknowledge that given the high variability typical of developmental
584 studies, we might have still been underpowered to detect additional sex differences in
585 our datasets.

586 Juvenile inhibition of the iCA1-mPFC pathway led to an opposite effect from that of
587 vCA1-mPFC on adult cognitive flexibility, facilitating ED set shifting performance. This
588 suggests that vCA1- and iCA1-mPFC pathways may exert competing and opposing
589 roles in the modulation of cognitive flexibility, a possibility that needs to be further
590 investigated. Strikingly, juvenile iCA1-mPFC inhibition impacted adult cognitive flexibility
591 in both males and females, whereas vCA1-mPFC juvenile inhibition only affected
592 females. This mirrors our anatomical and electrophysiological findings, whereby vCA1-
593 mPFC refinement was only seen in juvenile females, but was widespread across
594 metrics and sexes for the iCA1-mPFC pathway, reinforcing a correlation between the
595 timing of changes in pathway connectivity and sensitivity to disruption. Critically, this
596 pattern was also reflected in the effect of juvenile chronic inhibition on mPFC
597 spontaneous transmission, whereby juvenile vCA1-mPFC inhibition only reduced mPFC
598 transmission in females, but mPFC spontaneous transmission was altered in both sexes
599 following juvenile iCA1-mPFC inhibition, matching the behavioral alterations in ED set
600 shifting performance.

601 Although juvenile inhibition of the iCA1-mPFC pathway led to an enhancement in ED
602 set-shifting in both males and females, its consequences to PL spontaneous
603 transmission were sex-specific. This adds to a growing body of work identifying sex
604 differences in the neural basis of behavior, including in instances of equivalent

605 behavioral output across sexes[172–175]. Additionally, pubertal onset of psychiatric
606 disorders has been linked to changes in cognitive flexibility[176–179], as well as changes in
607 mPFC (and CA1[180]) perineuronal nets[181] and increased inhibition[178] in females, factors
608 known to modulate sensitive periods[182–184]. Given the earlier onset of puberty in female
609 mice relative to males[178,185], which spans our intervention window, it will be important to
610 uncover any potential effects of puberty on pathway-specific maturation and its
611 modulation of cognitive flexibility.

612 Previous studies had implicated mPFC function in the same ED set shifting task of
613 cognitive flexibility, with a key role for mPFC parvalbumin interneuron activity from P14-
614 P50 in adult ED set shifting performance[146]. While this timing overlaps with that of our
615 manipulation, the contribution of local mPFC interneurons to our findings is unknown.
616 Furthermore, inhibition of mediodorsal thalamus (MD) from P20-P50 leads to similar ED
617 set shifting impairments, which were accompanied by a reduction in mPFC sEPSC
618 frequency and in the density of thalamus-mPFC projections in adulthood[91], suggesting
619 that both CA1- and MD-mPFC pathways exert a developmental influence on adult
620 cognitive flexibility. Intriguingly, layer 2/3 PL pyramidal neurons receive convergent input
621 from both MD and vHPC, while input to interneurons is biased: parvalbumin
622 interneurons receive relatively more input from MD and VIP interneurons from the
623 vHPC[186]. The exact interplay of these pathways and their modulation of developmental
624 sensitivity to disruption should be further explored. Finally, a recent study showed that
625 systemic disruption of microglia activity from P28-P37 in mice led to changes in mPFC
626 network function and deficits in attentional set shifting rule acquisition and reversal
627 learning in adulthood[187]. While ED set shifting was not assessed, this suggests the

628 timing of this sensitive period might extend into adolescence, while raising the question
629 of whether HPC input to mPFC is sensitive to microglial manipulation. Importantly, this
630 developmental timeline is also consistent with that reported for the effects of
631 amphetamine (P22-P31) on adult mPFC dopaminergic innervation and behavioral
632 inhibition[141,188], further establishing this period as one of broad sensitivity to mPFC-
633 related circuit function and behavior.

634 While these studies, together with ours, support a sensitive period from juvenility to
635 adolescence for mPFC-dependent cognitive function in adulthood, neonatal mPFC
636 disruptions have also been linked to behavioral deficits. Transient optogenetic activation
637 of mPFC from P7-11 leads to social, recognition and working memory deficits in
638 juvenility and adolescence, which are accompanied by changes in mPFC morphology,
639 electrophysiology and oscillations[189]. Additionally, serotonin transporter blockade from
640 P2-P11 disrupts mPFC morphology, neuronal excitability and anxiety- and depression-
641 like behavior[73]. Interestingly, the same group recently implicated serotonergic input to
642 the mPFC in ED set shifting[190], urging future research to explore the degree of overlap
643 (if any) between serotonergic and v/iCA1 terminals onto mPFC pyramidal neurons.
644 Ultimately, as research continues to refine knowledge of the topography and function of
645 HPC projections[113,142], the sex- and pathway-specific interrogation of the postnatal
646 development of HPC pathways adds a crucial layer to improving our understanding of
647 brain-behavior relationships and their contribution to the physiology of emotional and
648 cognitive function across the lifespan.

649

650 **Figures and Figure Legends:**

651

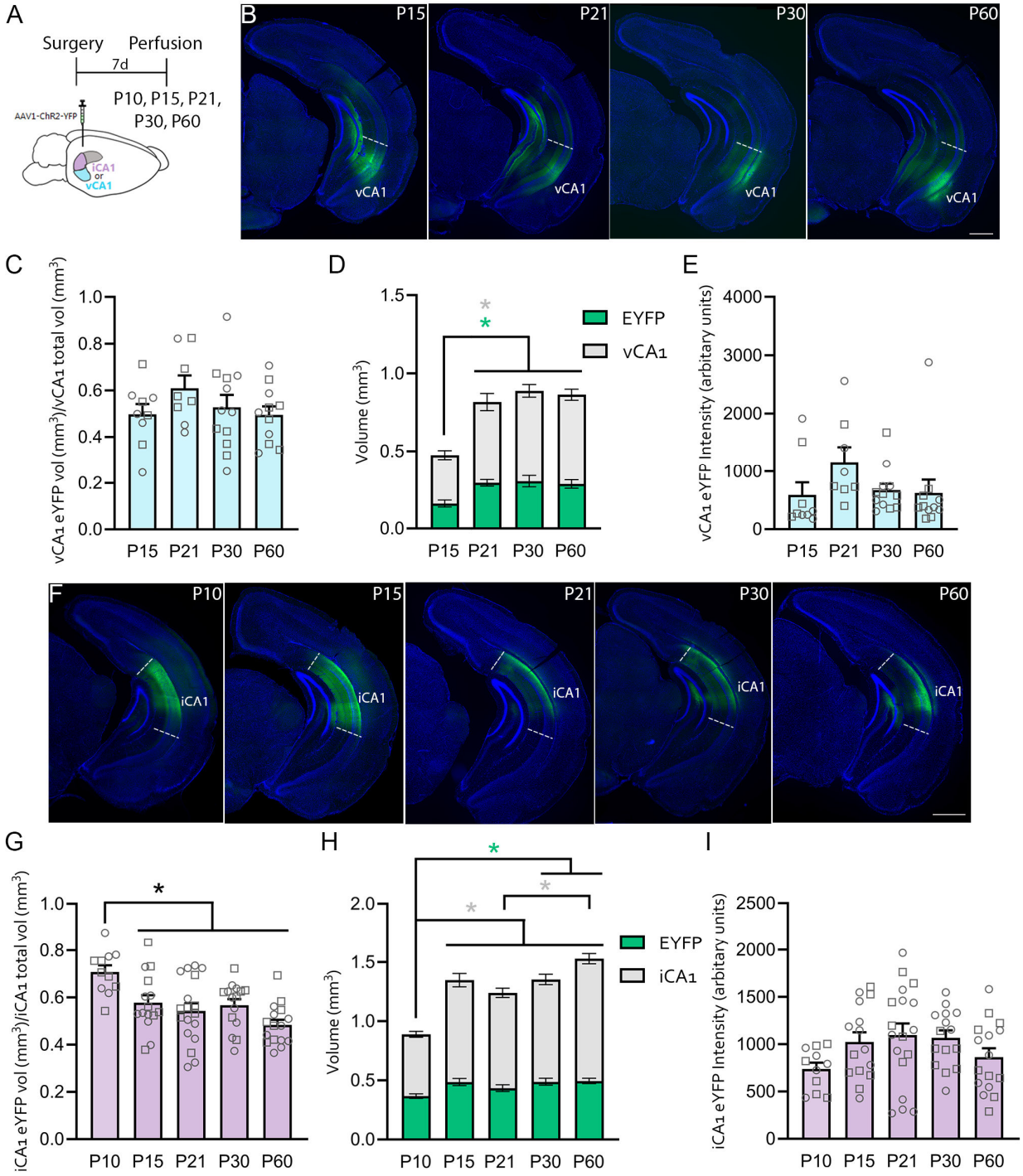

652

653 **Figure 1. Targeting vCA1 and iCA1 across ages. A.** C57BL/6J mice were injected
654 with AAV-ChR2-YFP virus in either the vCA1 (**B-E**) or iCA1 (**F-I**) and perfused seven

655 days later at P10, P15, P21, P30 or P60 for tissue and image processing. **B**. Sample
656 images of AAV1-ChR2-EYFP infusion at the vCA1 in P15, P21, P30 and P60 mice. **C**.
657 Estimated proportion of total vCA1 volume (mm^3) with EYFP infection for each age
658 group. **D**. Estimated total vCA1 volume (grey) and EYFP infected vCA1 volume (green)
659 for all age groups. **E**. Average intensity of infected EYFP vCA1 area for each age group.
660 **F**. Sample images of AAV1-ChR2-EYFP infusion at the iCA1 in P10, P15, P21, P30 and
661 P60 mice. **G**. Estimated proportion of total iCA1 volume (mm^3) with EYFP infection for
662 each age group. **H**. Estimated total iCA1 volume (grey) and EYFP infected iCA1 volume
663 (green) for all age groups. **I**. Average intensity of infected EYFP iCA1 area for each age
664 group. Individual female datapoints are represented as circles, and males as squares.
665 Scale bars: 500μm. * $p < 0.05$. Grey and green asterisks in **D** and **H** represent statistical
666 significance in the total region volume and EYFP volume datasets, respectively. For full
667 n values and break-down of all figures, refer to Table S1.

668

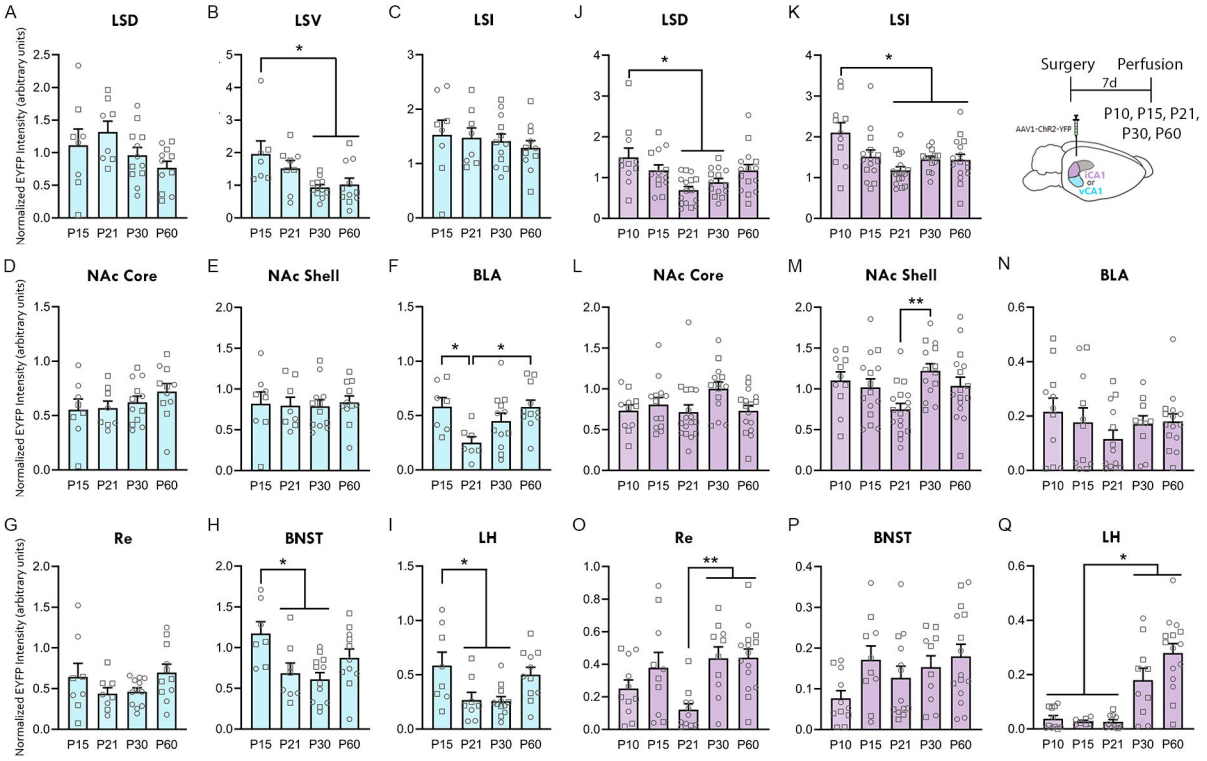

669

670 **Figure 2. Pathway-specific developmental changes in vCA1 and iCA1 terminal**
671 **density.** C57BL/6J mice were injected with AAV-ChR2-YFP virus in the vCA1 (**A-I**) or
672 the iCA1 (**J-Q**) and perfused seven days later at P10, P15, P21, P30 or P60 for tissue
673 and image processing. **A-I**. Normalized average vCA1 terminal intensity across ages at
674 the dorsal lateral septum (LSD; **A**), ventral lateral septum (LSV; **B**), intermediate lateral
675 septum (LSI; **C**), nucleus accumbens (NAc) core (**D**) and shell (**E**); basolateral
676 amygdala (BLA; **F**), thalamic nucleus reuniens (Re; **G**), bed nucleus of the stria
677 terminalis (BNST; **H**), and lateral hypothalamus (LH; **I**). **J-Q**. Normalized average iCA1

678 terminal intensity across ages at the LSD (**J**), LSI (**K**), NAc core (**L**) and shell (**M**), BLA
679 (**N**), Re (**O**), BNST (**P**), and LH (**Q**). Individual female datapoints are represented as
680 circles, and males as squares. *$p<0.05$. **$p<0.01$.

681

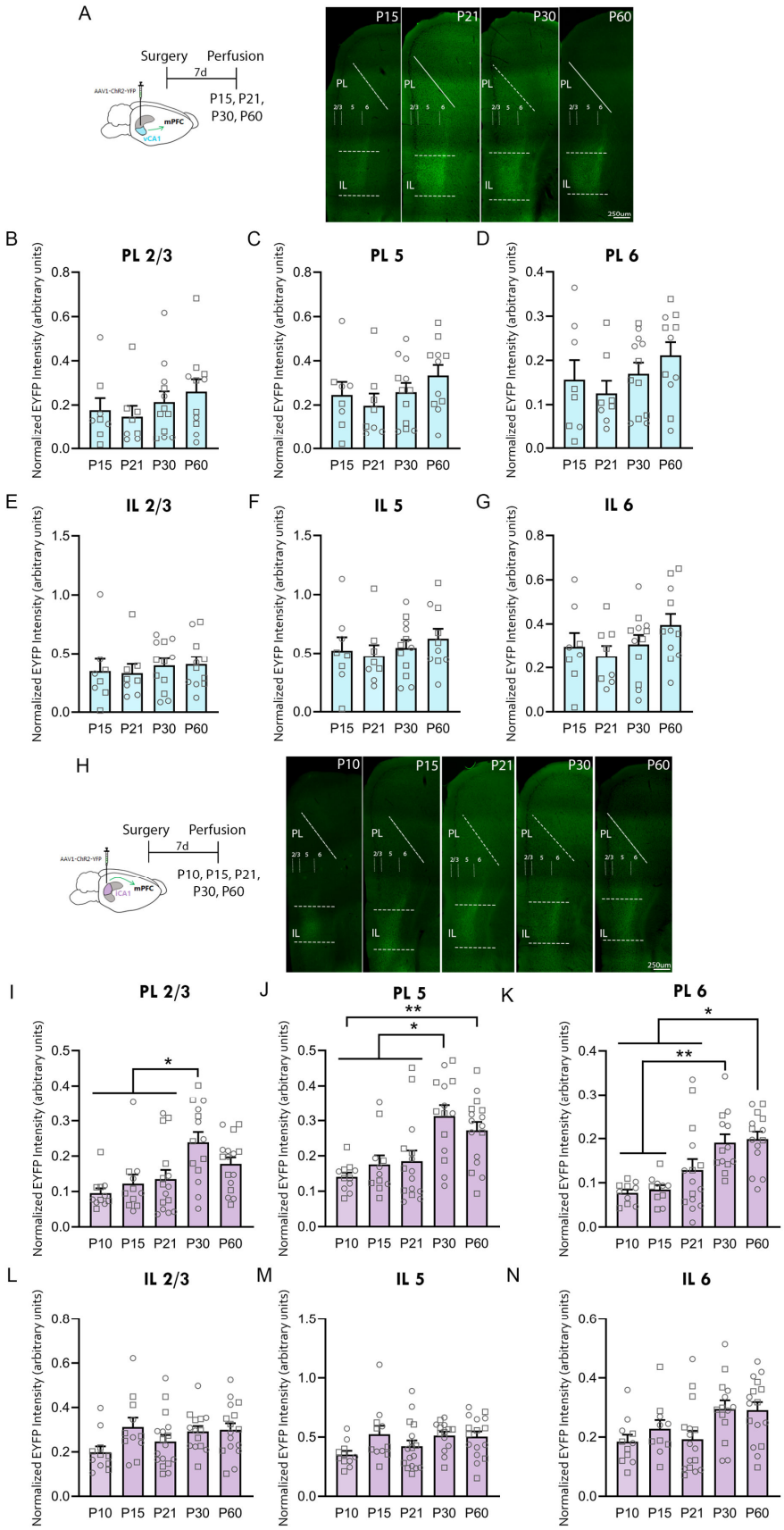
A
Surgery
Perfusion
7d
P15, P21, P30, P60
AAV1-ChR2-YFP
mPFC
vCA1
P15
P21
P30
P60
PL
IL
250um
B
PL 2/3
C
PL 5
D
PL 6
E
IL 2/3
F
IL 5
G
IL 6
Normalized EYFP Intensity (arbitrary units)
P15 P21 P30 P60
H
Surgery
Perfusion
7d
P10, P15, P21, P30, P60
P10
I
PL 2/3
J
PL 5
K
PL 6
L
IL 2/3
M
IL 5
N
IL 6
P10 P15 P21 P30 P60

682

683 **Figure 3. vCA1 terminal density is stable in PL and IL across postnatal**
684 **development, but iCA1 terminal density increases in PL starting at adolescence.**
685 **A**. *Left*: Experimental design for the vCA1 experiments. C57BL/6J mice were injected
686 with AAV-ChR2-YFP virus in the vCA1 and perfused seven days later at P15, P21, P30
687 or P60 for tissue and image processing. *Right*: Sample images of vCA1 projections
688 present at the medial prefrontal cortex in P15, P21, P30 and P60 mice (numbers
689 indicate cortical layers). **B-D**. Quantification of vCA1 terminal intensity across ages in
690 PL layers 2/3 (**B**), 5 (**C**) and 6 (**D**)**. E-G**. Average vCA1 terminal intensity for all age
691 groups at IL layers 2/3 (**E**), 5 (**F**) and 6 (**G**). **H**. *Left:* Experimental design for the iCA1
692 experiments. C57BL/6J mice were injected with AAV-ChR2-YFP virus in the iCA1 and
693 perfused seven days later at P10, P15, P21, P30 or P60 for tissue and image
694 processing. *Right*: Sample images of iCA1 projections present at the mPFC. **I-K**. Age-
695 dependent differences in iCA1 terminal intensity in PL layers 2/3 (**I**), 5 (**J**) and 6 (**K**)**. L-**
696 **N**. Average iCA1 terminal intensity for all age groups at IL layers 2/3 (**L**), 5 (**M**) and 6
697 (**N**). Individual female datapoints are represented as circles, and males as squares.
698 Scale bar: 250μm. *p<0.05, ** p<0.01. PL = prelimbic cortex. IL = infralimbic cortex.

699

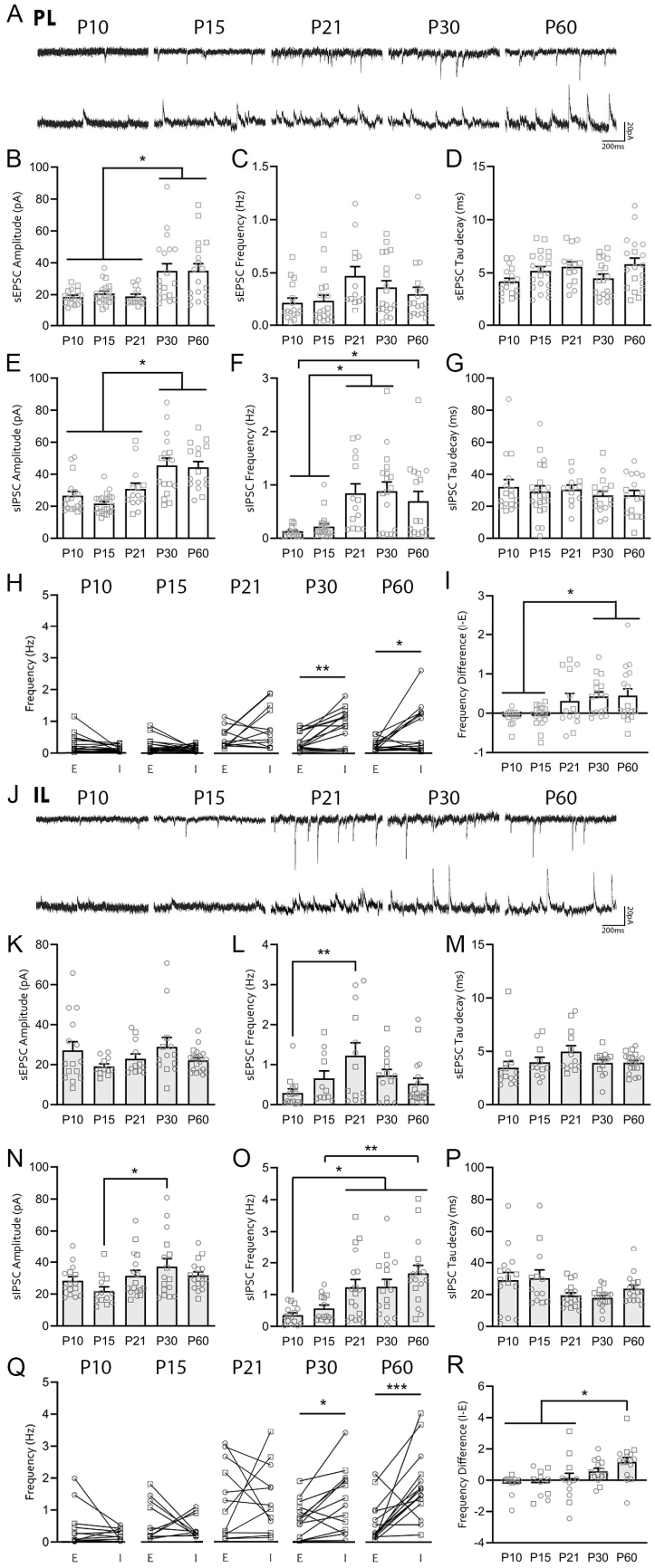
A PL
P10
P15
P21
P30
P60
20pA
200ms
B
sEPSC Amplitude (pA)
C
sEPSC Frequency (Hz)
D
sEPSC Tau decay (ms)
E
sIPSC Amplitude (pA)
F
sIPSC Frequency (Hz)
G
sIPSC Tau decay (ms)
H
Frequency (Hz)
E
I
I
Frequency Difference (I-E)
J IL
K
L
M
N
O
P
Q
R

700

701 **Figure 4. Maturation of PL and IL layer 5 Pyramidal Cell Spontaneous Activity. A-I**.
702 Age-dependent changes in PL layer 5 pyramidal neuron spontaneous excitatory and
703 inhibitory postsynaptic currents (sEPSCs and sIPSCs) from P10 to P60. Example traces
704 **(A),** sEPSC amplitude (**B**), frequency (**C**) and tau decay (**D**). sIPSC amplitude (**E**),
705 frequency (**F**) and tau decay (**G**). **H**. Within-cell comparison of sEPSC and sIPSC
706 frequencies. **I**. Spontaneous I-E frequency difference (calculated by subtracting sEPSC
707 frequency from sIPSC frequency). **J-R**. Maturation of IL layer 5 Spontaneous Activity.
708 Example traces (**J**)**,** sEPSC amplitude (**K**), frequency (**L**) and tau decay (**M**). IL sIPSC
709 amplitude (**N**), frequency (**O**) and tau decay (**P**). **Q**. Within-cell comparison of relative
710 sEPSC and sIPSC frequencies. **R.** Spontaneous I-E frequency difference. Individual
711 female datapoints are represented as circles, and males as squares. ***** $p < 0.05$ ******
712 $p<0.01$ ******* $p<0.001$.

713

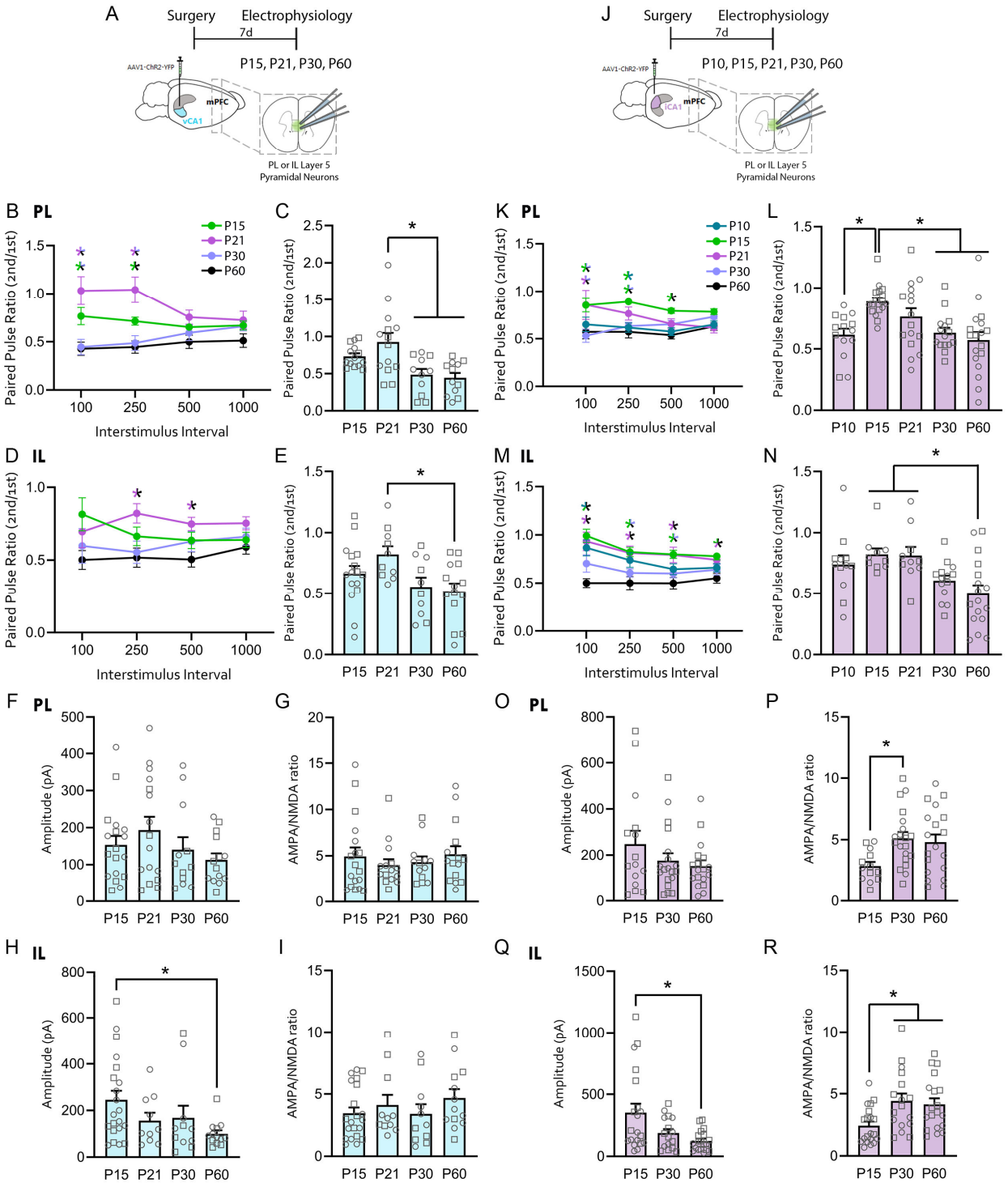

714

715

716

717 **Figure 5. Asynchronous pre- and postsynaptic strengthening of vCA1- and iCA1-**
718 **PL and IL synapses.** C57BL/6J mice were injected with AAV-ChR2-YFP virus in the

vCA1 (**A-I**) or the iCA1 (**J-R**) and seven days later at P10 (iCA1), P15, P21, P30 or P60 underwent patch clamp recordings from PL or IL layer 5 pyramidal neurons upon blue light LED stimulation. **A**. Experimental design for vCA1 experiments. **B-E**. Comparison of paired pulse ratio (second/first response) in PL layer 5 pyramidal neurons across intervals (**B**) and at 250ms interstimulus interval (**C**). **D-E.** Paired pulse ratios from IL layer 5 pyramidal neurons across intervals (**D**) and with 250ms interval (**E**). **F-G**. vCA1-PL layer 5 AMPAR current amplitude (**F**) and AMPA:NMDA ratios (**G**) across ages. **H-I.** vCA1-IL AMPAR amplitudes (**H**) and AMPA:NMDA ratio (**I**). **J**. Experimental design for iCA1 experiments. **K-L**. Paired pulse ratios in iCA1-PL synapses across interstimulus intervals (**K**) and at 250ms interstimulus interval (**L**). **M-N.** Paired pulse ratios in iCA1-IL synapses across intervals (**M**) and with 250ms interval (**N**). **O-R**. iCA1-PL AMPAR current amplitude (**O**) and AMPA:NMDA ratios (**P**). **Q-R**. iCA1-IL AMPAR current amplitude (**Q**) and AMPA:NMDA ratios (**R**). Individual female datapoints are represented as circles, and males as squares. *p <0.05. * Represents a difference between P21 and P30/P60; * between P15 and P60; * between P15 and P10; * between P10/P15 and P60; * between P15 and P30/P60; * between P15/P21 and P60; * between P21 and P60, and * between P15 and P21.

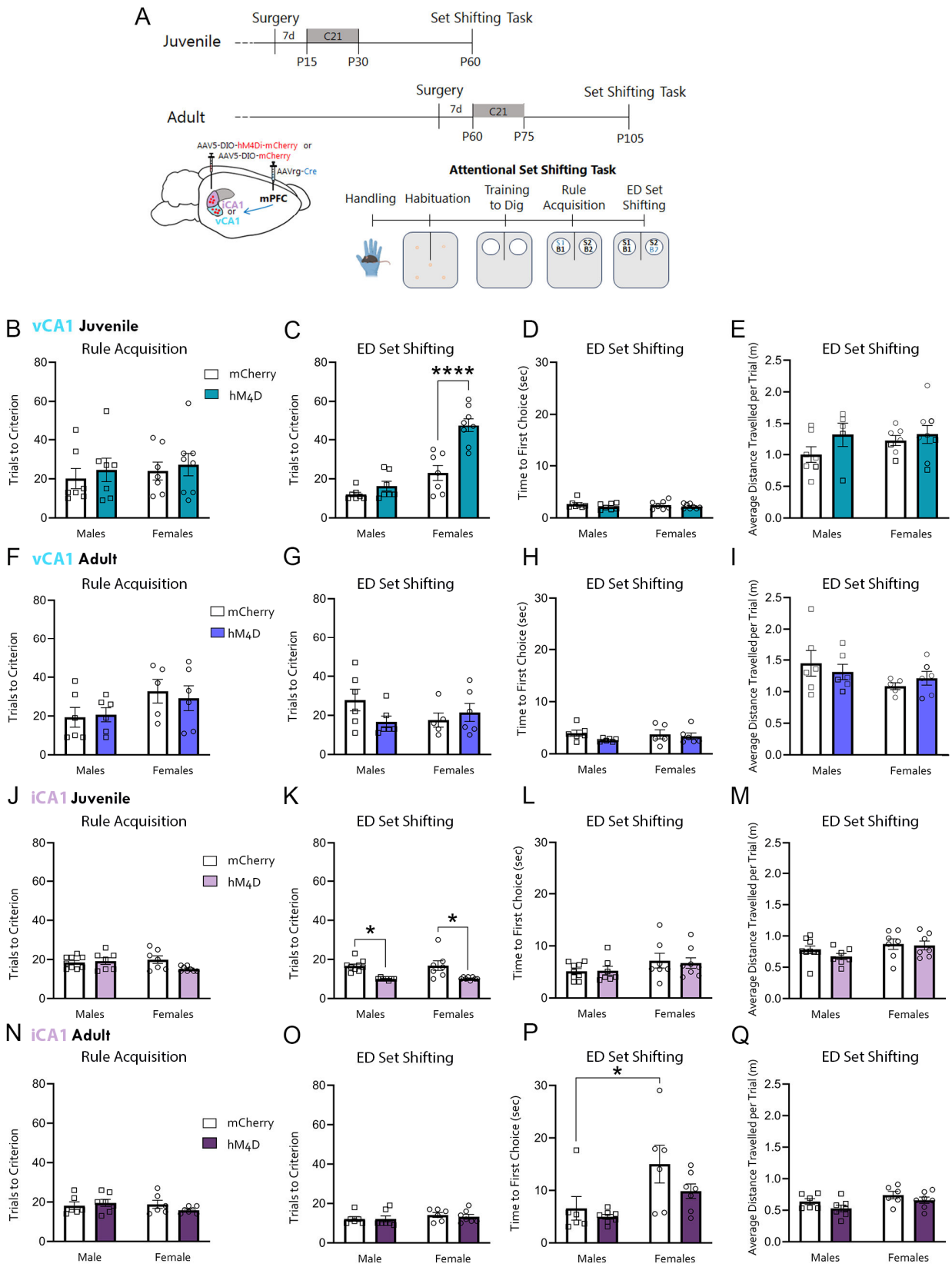
A
Juvenile
Surgery
7d
C21
Set Shifting Task
P15
P30
P60
Adult
Surgery
7d
C21
Set Shifting Task
P60
P75
P105
AAV5-DIO-hM4Di-mCherry or
AAV5-DIO-mCherry
AAVrg-Cre
mPFC
iCA1
or
vCA1
Attentional Set Shifting Task
Handling
Habituation
Training to Dig
Rule Acquisition
ED Set Shifting
B vCA1 Juvenile
Rule Acquisition
mCherry
hM4D
Trials to Criterion
Males
Females
C
ED Set Shifting
****
D
ED Set Shifting
Time to First Choice (sec)
E
ED Set Shifting
Average Distance Travelled per Trial (m)
F vCA1 Adult
G
H
I
J iCA1 Juvenile
K
*
*
L
M
N iCA1 Adult
Male
Female
O
P
*
Q

739 **Figure 6. vCA1- and iCA1-mPFC inhibition during juvenility, but not adulthood,**
740 **impacts extradimensional set shifting. A.** Experimental design. Mice were injected
741 with a retrograde AAV expressing Cre recombinase (AAVrg-Cre) in the mPFC and Cre-
742 dependent hM4D or mCherry (AAV-DIO-hM4D-mCherry or AAV-DIO-mCherry) in either
743 the vCA1 or iCA1 7d prior to chronic treatment with the DREADD agonist C21 for 15d
744 either during the *juvenile* period (from P15-P30) or in *adulthood* (separate cohort
745 receiving equivalent C21 injections from P60-P75). 30d later, animals underwent
746 attentional set shifting[90,91]. Following handling, habituation and training to dig sessions,
747 animals learned an association (rule acquisition) between a scent and a food reward
748 (rewarded contingency marked in blue). The next day, animals underwent an
749 extradimensional (ED) set shifting test in which the reward was paired with the bedding
750 type. All groups underwent set shifting in adulthood in the absence of C21. **B-E**. vCA1
751 juvenile cohort. Number of trials to criterion at rule acquisition (**B**) and ED set shifting
752 (**C**). Time to first choice (**D**) and distance travelled (**E**) during ED set shifting. **F-I**. vCA1
753 adult cohort. Number of trials to criterion at rule acquisition (**F**) and ED set shifting (**G**).
754 Time to first choice (**H**) and distance travelled (**I**) during ED set shifting. **J-M**. iCA1
755 juvenile cohort. Number of trials to criterion at rule acquisition (**J**) and ED set shifting
756 (**K**). Time to first choice (**L**) and distance travelled (**M**) during ED set shifting. **N-Q**. iCA1
757 adult cohort. Number of trials to criterion at rule acquisition (**N**) and ED set shifting (**O**).
758 Time to first choice (**P**) and distance travelled (**Q**) during ED set shifting. Individual
759 female datapoints are represented as circles, and males as squares. *$p<0.05$,
760 ****$p<0.0001$.

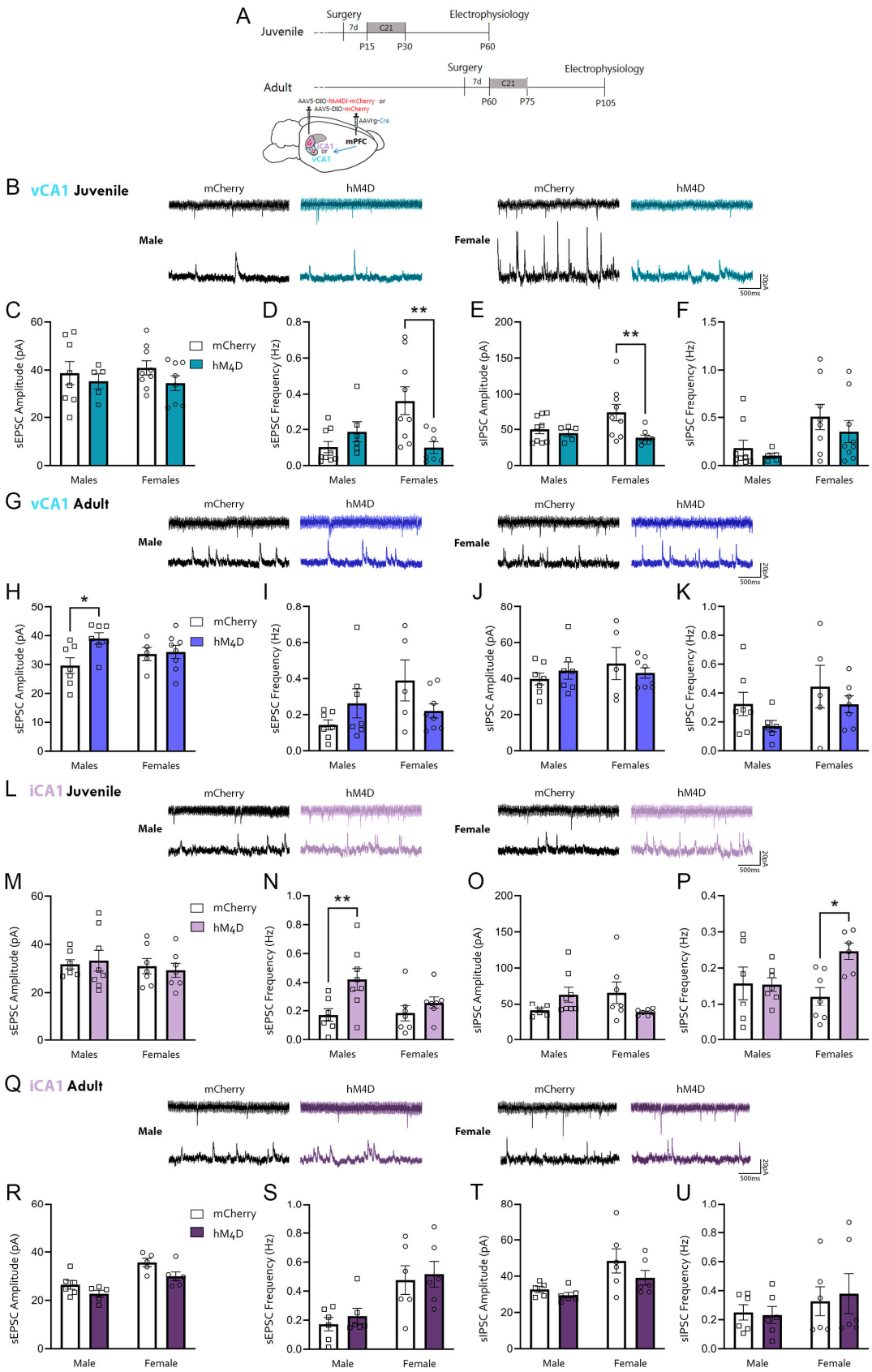
A
Juvenile
Surgery
7d
C21
Electrophysiology
P15
P30
P60
Adult
Surgery
7d
C21
Electrophysiology
P60
P75
P105
AAV5-DIO-hM4Di-mCherry or
AAV5-DIO-mCherry
AAVrg-Cre
mPFC
iCA1
or
vCA1
B vCA1 Juvenile
mCherry
hM4D
Male
Female
20pA
500ms
C
D
E
F
sEPSC Amplitude (pA)
sEPSC Frequency (Hz)
sIPSC Amplitude (pA)
sIPSC Frequency (Hz)
mCherry
hM4D
Males
Females
**
**
G vCA1 Adult
H
I
J
K
*
L iCA1 Juvenile
M
N
O
P
**
*
Q iCA1 Adult
R
S
T
U
Male
Female

761

762 **Figure 7. vCA1- and iCA1-mPFC juvenile inhibition impacts PL layer 5 Pyramidal**
763 **Cell Spontaneous Activity. A.** Experimental design. Mice were injected with a
764 retrograde AAV expressing Cre recombinase (AAVrg-Cre) in the mPFC and Cre-
765 dependent hM4D or mCherry (AAV-DIO-hM4D-mCherry or AAV-DIO-mCherry) in either
766 the vCA1 or iCA1 7d prior to chronic treatment with the DREADD agonist C21 for 15d
767 either during the *juvenile* period (from P15-P30) or in *adulthood* (separate cohort
768 receiving equivalent C21 injections from P60-P75). Approximately 30d later, animals
769 underwent patch clamp recordings from PL layer 5 pyramidal neurons in the absence of
770 C21. **B-F**. vCA1 juvenile cohort. Example sEPSC (*top*) and sIPSC (*bottom*) traces (**B**).
771 sEPSC amplitude (**C**) and frequency (**D**). sIPSC amplitude (**E**) and frequency (**F**). **G-K**.
772 vCA1 adult cohort. Example traces (**G**), sEPSC amplitude (**H**) and frequency (**I**), sIPSC
773 amplitude (**J**) and frequency (**K**). **L-P**. iCA1 juvenile cohort. Example traces (**L**), sEPSC
774 amplitude (**M**) and frequency (**N**), sIPSC amplitude (**O**) and frequency (**P**). **Q-U**. iCA1
775 adult cohort. Example traces (**Q**), sEPSC amplitude (**R**) and frequency (**S**), sIPSC
776 amplitude (**T**) and frequency (**U**). Individual female datapoints are represented as
777 circles, and males as squares. *p<0.05, ** p<0.01.

778

779 **Methods**

780 Animals

781 C57BL/6J (Jackson Laboratory) mice were bred at the University of Toronto
782 Scarborough and kept on a 12h light/dark cycle (lights on at 07:00 h) in a standard static
783 cage on ¼" corncob bedding with access to food and water *ad libitum*. Date of birth was
784 designated postnatal day (P)0, with litter sizes ranging from 2 to 11 pups. At 21 days
785 (P21) mice were weaned and housed in same-sex littermate groups of 2 to 5 mice.
786 Adolescence was considered at P30[191], consistent with our previous work[101,154,192].
787 Littermates were randomly assigned to experimental groups, with each litter distributed
788 across ages tested counterbalanced for sex. All experiments were conducted during the
789 light cycle. Approximately equal numbers of females and males were used for all
790 experiments. All animal procedures were approved by the Animal Care Committee at
791 the University of Toronto.

792 Stereotaxic surgery and viral injections

793 C57Bl/6J mice underwent stereotaxic surgery at P3, P8, P14, P23 or P53. 0.12-0.25μL
794 of AAV1-CaMKIIa-hChR2(H134R)-EYFP virus was infused at the iCA1 bilaterally for
795 each age group (P3: AP-2.5, ML-/+2.65, DV-2.5; P8: AP-2.60, ML-/+3.15, DV-3.00;
796 P14: AP-2.65, ML-/+ 3.2, DV-3.00; P23: AP-2.7, ML-/+3.4, DV-3.00; P53: AP-2.75, ML-
797 /+3.6, DV-3.00). For vCA1 experiments, 0.12-0.2μL of AAV1-CaMKIIa-hChR2(H134R)-
798 EYFP virus was infused at the vCA1 bilaterally at P8, P14, P23 or P53 (P8: AP-2.46,
799 ML-/+3.05, DV-4.60; P14: AP-1.9, ML-/+ 3.1, DV-4.6; P23: AP-2.42, ML-/+3.1, DV-4.60;
800 P53: AP-2.53, ML-/+3.25, DV-4.5). For dCA1 experiments, 0.2uL of AAV1-CaMKIIa-
801 hChR2(H134R)-EYFP virus was infused at the dCA1 bilaterally at P53 (AP-2.1, ML-
802 /+1.50, DV-1.50). Hypothermia was used as an anesthetic for surgeries taken place at
803 P3. Mice older than P8 were injected intraperitoneally (i.p.) with a combination of
804 ketamine (100 mg/kg) and xylazine (5 mg/kg) to induce anesthesia. Once anesthetized,
805 the head was shaved and swabbed with iodine followed by 70% ethanol. Tear gel
806 (Alcon) was applied to the eyes to prevent dehydration. Mice were then secured in a
807 rodent stereotaxic apparatus (Stoelting) using ear bars. Body temperature was
808 maintained throughout surgery with a heating blanket. An incision was made down the
809 midline of the scalp using a scalpel, the connective tissue was excised, and then the
810 skull was cleaned with sterile phosphate buffered saline (PBS, pH=7.4). An autoclaved
811 cotton-tip applicator was briefly submerged in 30% hydrogen peroxide and gently
812 applied to the skull surface to identify bregma. After surgery, mice recovered for one
813 week and then were transcardially perfused or underwent slice electrophysiology
814 (details described below). For the retrograde tracing surgeries, mice at P0, P5 or aged

815 8-9 weeks underwent stereotaxic surgery (as above) infusing, bilaterally, red Lumafluor
816 RetroBeads™ at the mPFC (P0: AP+0.3, ML-/+0.2, DV-0.75; P5: AP+1.07, ML-/+0.25,
817 DV-2.6; Adult: AP+2.0, ML-/+0.3, DV-2.8). Five days after surgery, mice underwent
818 transcardial perfusion (details described below). For the set shifting experiments, mice
819 at P8 or P53 underwent stereotaxic surgery (as described above) infusing bilaterally,
820 pAAV5-hSyn-DIO-hM4D(Gi)-mCherry or pAAV5-hSyn-DIO-mCherry at the vCA1or iCA1
821 (coordinates for P8 and P53 above) and pENN-AAV-hSyn-Cre-WPRE-hGH
822 (Retrograde) at the mPFC (P8: AP+1.52, ML-/+0.26, DV-2.5; P53: AP+2.0, ML-/+0.3,
823 DV-2.8). After surgery, mice recovered for one week prior to commencing chronic C21
824 injections (procedure described below). We chose a chemogenetic intersectional
825 approach in these experiments because of challenges related to optic fiber implantation
826 in very young mice (in the juvenile group), in addition to limitations of chronic light
827 stimulation in optogenetic experiments.

828 Perfusions and sectioning

829 Mice were injected with Avertin (250mg/kg, i.p.) and once under deep anesthesia,
830 transcardially perfused with approximately 50mL of room temperature 0.1M PBS
831 (pH=7.4), followed by approximately 80mL of cold 4% paraformaldehyde (PFA). Brains
832 were extracted and stored overnight at 4°C in 4% PFA. Brains were subsequently
833 sectioned at 50µm in the coronal plane (VT1000, Leica) and stored at -20 °C in a
834 cryoprotectant solution comprised of 60% glycerol and 0.01% sodium azide in PBS.

835 Immunohistochemistry

836 Immunostaining was performed on free floating sections. Sections were washed in 0.1M
837 PBS (3 x 5 min each) and then incubated in blocking solution comprising 5% normal
838 goat serum and 0.25% Triton X-100 in 0.1M PBS for 30 min. For the amplified dCA1,
839 vCA1 and iCA1 brains, amplification of the viral signal was achieved by incubating
840 sections with polyclonal chicken anti-GFP (1:1000, #ab13970; Abcam, RRID:
841 AB_300798) primary antibody diluted in blocking solution. Sections were incubated
842 overnight at 4 °C on a rotary shaker under gentle agitation. On the following morning,
843 sections were incubated in goat anti-chicken Alexa 488 (1:1000, #A11039, Invitrogen,
844 RRID: AB_2534096) secondary antibody for 2 hours and Hoechst 33342 nuclear dye
845 (1:1000 diluted in 0.1M PBS; #H1399; ThermoFisher). Sections were then rinsed in
846 0.1M PBS, mounted onto gelatin-coated slides and coverslipped with Permafluor anti-
847 fade mounting medium (#TA030FM; Thermo Scientific).

848 Anatomical maturation analysis

849 Brains were sectioned (50µm thickness) with a VT1000S vibratome (Leica). All sections
850 were stained with nuclear dye Hoechst 33342 (1:1000) for 10 min at room temperature.
851 Sections were mounted onto slides, air dried, and coverslipped with anti-fade mounting
852 medium (as described above) and imaged using a Nikon Eclipse Ni-U Upright
853 epifluorescent microscope. iCA1 and vCA1 projection-associated EYFP fluorescence
854 was quantified by measuring average pixel intensity for each region of interest and
855 subtracting the background/basal measure of intensity. For the vCA1/iCA1
856 measurements (Figure 1), high fluorescence intensity at the injection site prevented
857 quantification of individual neurons. The terminal density analyses (Figures 2, 3, S1)
858 exclusively captured axon fluorescence, as we did not see cell bodies in any of the

859 terminal target images. Internal baseline measures of intensity for each section were
860 taken from the motor cortex/frontal associative cortex which are devoid of temporal
861 hippocampal projections[114]. An average intensity difference was calculated from both
862 hemispheres using ImageJ/FIJI software (NIH, MD, USA;
863 https://imagej.net/software/fiji/). Regions of interest included: the prelimbic cortex (PL)
864 (layer 2/3, 5 and 6), infralimbic cortex (IL) (layer 2/3, 5 and 6), nucleus accumbens
865 (NAc) (shell and core), lateral septum (LS) (dorsal, ventral and intermediate nucleus),
866 basolateral amygdala (BLA), lateral hypothalamus (LH), thalamic nucleus reuniens (Re)
867 and the bed nucleus of the stria terminalis (BNST). Whole area intensity was measured
868 for each region. Comparisons were made of vCA1/iCA1 projection-associated EYFP
869 intensity at these regions among the different age groups. All calculated intensities were
870 normalized with EYFP intensity in vCA1 or iCA1 injection site.

871 To ensure viral spread is restricted only to, and covers the whole of the vCA1 or iCA1,
872 the Cavalieri method [($V_c = d(\Sigma(y_i))$), where V_c = estimated volume (mm^3), d = distance
873 between sections (μm) and y = area of EYFP infection or vCA1/iCA1 per section (mm^2)]
874 was used to estimate, for each age, viral spread and total vCA1/iCA1 volume. The iCA1
875 is defined as the dorsal CA1 ($dCA1^i$) region (pyramidal, oriens and radiatum layers) that
876 begins from bregma -2.70mm and terminates at -3.88mm labelled in Franklin & Paxinos
877 mouse atlas[193]. For sections that do not have the CA2 region that easily delineates the
878 $dCA1^i$ on the dorsal-ventral axis within bregma -2.70 to -3.88mm, the $dCA1^i$ consisted of
879 the CA1 area above the rhinal fissure/bottom limit of the perirhinal cortex[193]. This
880 boundary follows the lower border of the intermediate CA1 set by Dong et al. (2009) and
881 Fanselow & Dong (2010). Since these authors found that their iCA1 region and

882 temporal/posterior dCA1 region follow the same pattern of gene expression[22], for this
883 study, the iCA1 encompasses both Dong et al. (2009)'s posterior dCA1 and iCA1.
884 Estimated volume of EYFP and vCA1/iCA1 were compared between each age group to
885 corroborate the reduction of hippocampal mass and the restriction of viral spread at
886 earlier ages[101]. Results are expressed as percentage of estimated EYFP volume and
887 vCA1/iCA1 volume.

888 For the quantification of cells infused with Lumafluor RetroBeads™ cells (Figure S3),
889 images were obtained a Nikon Eclipse Ni-U Upright epifluorescent microscope and
890 manually counted using ImageJ/FIJI software (NIH, MD, USA;
891 https://imagej.net/software/fiji/).

892 Slice electrophysiology

893 Mice were anesthetized with isoflurane and perfused transcardially with ice-cold (0°C–
894 4°C) sucrose solution composed of (in mM): 197 sucrose, 11 glucose, 2.5 KCl, 1.25
895 NaH2PO4, 25 NaHCO3, 0.4 ascorbate, 1 CaCl2, 4 MgCl2 and 2 Na pyruvate. Acute
896 350 μm coronal slices of PFC were obtained from dissected brains using a VT1000S
897 vibratome (Leica) and then incubated at 35°C for 25 min in the same solution, but with
898 50% standard artificial cerebral spinal fluid (ACSF) composed of (in mM): 120 NaCl, 2.5
899 KCl, 1.25 NaH2PO4, 25 NaHCO3, 11 glucose, 2 CaCl2, 1 MgCl2 and 2 Na pyruvate.
900 Following recovery, slices were maintained at room temperature in standard ACSF.
901 Whole-cell voltage-clamp recordings were obtained from principal pyramidal neurons in
902 layer 5 PL or IL using borosilicate glass electrodes (3–5 MΩ). Electrode internal solution
903 was composed of (in mM) of the following: 130 Cs-methanesulfonate, 10 HEPES, 0.5

904 EGTA, 8 NaCl, 4 Mg-ATP, 1 QX-314, 10 Na-phosphocreatine, and 0.4 Na-GTP.
905 Pyramidal excitatory neurons in the mPFC were discriminated on the basis of soma
906 size, high capacitance (>200 pF), and slow EPSC kinetics, under the rationale that no
907 interneuron subtypes possess all three of these characteristics. CA1 axon terminals
908 were stimulated using illumination with a digital multimirror device (Polygon400,
909 Mightex) and a TTL-pulsed microscope objective-coupled light-emitting diode (LED, 470
910 nm, 14 mW/mm2, Mightex). This pulse intensity evoked maximal response amplitudes
911 at all ages. For analysis of AMPA/NMDA ratios, we applied 1 μM TTX (#HB1035,
912 HelloBio) and 100 μM 4-AP (#AB120122, Abcam) for more stringent isolation of
913 monosynaptic transmission [101,194,195]. Paired pulse evoked EPSC and spontaneous
914 EPSCs and IPSCs were conducted in standard ACSF described above. Paired pulse
915 evoked EPSC were recorded using a low chloride internal (TEA-Cl 5mM). Data were
916 low-pass filtered at 3 kHz (evoked) and 10 kHz (spontaneous) and acquired at 10 kHz
917 using Multiclamp 700B and pClamp 10 (Molecular Devices). All stimulation was
918 conducted at 0.1 Hz to avoid inducing synaptic plasticity. Series and membrane
919 resistance was continuously monitored, and recordings were discarded when these
920 measurements changed by >20%. Recordings in which series resistance exceeded 25
921 MΩ were rejected. Detection and analysis of sEPSCs and sIPSCs were performed blind
922 to experimental group using MiniAnalysis (Synaptosoft). EPSC decay time constants (τ
923 decay) were obtained by standard exponential curve fitting of averaged current traces in
924 Clampfit (Molecular Devices). AMPA/NMDA ratio was calculated as the peak EPSC at -
925 70 mV divided by the EPSC amplitude at 100ms after current onset at +40 mV[101,194].

926 <u>C21 injections</u>

927 Animals were injected for 16 days consecutively with DREADD agonist compound 21
928 (C21; 2mg/kg, 0.5mg/mL, i.p.; #HB6124; HelloBio)[131], twice a day[91], once at 8:30 am ±
929 1 hour and once at 4:30 pm ± 1 hour, ensuring an 8-hour gap in between. The juvenile
930 group was injected from P15-P30, and the adult group was injected from P60-P75.
931 These cohorts underwent either attentional set shifting or slice electrophysiology (whole
932 cell patch clamp recordings of sEPSCs and sIPSCs as described above) 30d later in the
933 absence of C21.

934 Behavioral testing

935 *Attentional Set Shifting Task*

936 *Apparatus:* A rectangular chamber made of white plexiglass (14.5 cm x 16.5 cm) was
937 separated by a 20 cm long x 16.5 cm wide x 0.5 cm thick plexiglass wall with two 19.2
938 cm wide x 17.8 cm long adjoining sliding doors on either lateral side to enclose the
939 mouse in the left or right upper quadrant. The apparatus was elevated 41 cm off the
940 floor with an Imaging Source DMK 22AUC03 1.1.3 IR camera mounted 88.4 cm directly
941 above it using a wall mount rack. An external LED lamp (280 Lux) was positioned
942 adjacent to the camera and 87.4 cm above the chamber to evenly distribute light. Two
943 round ceramic saucers each measuring 8.9 cm in diameter were placed in the chamber
944 at each of the quadrants during testing (at a 2.8 cm distance from each lateral wall and
945 7.6 cm away from the sliding door). The saucers were filled with one of two types of
946 bedding [counterbalanced; bark (Zoo Med Repti Bark) or cellulose paper (Biofresh 1/8"
947 Pelleted Cellulose) bedding], mixed with either a garlic or cinnamon powder
948 (McCormick), one of which predicted the reward location. Four different variations of

949 scent–bedding mixtures were used: bark–cinnamon, bark–garlic, paper–cinnamon and
950 paper–garlic.

951 *Procedure:* We used a variation of the protocol described by the Kellendonk group[90,91].
952 Animals were assessed in adulthood at P56-P61 for the juvenile group and at P101-
953 P106 for the adult group. Animals started undergoing food deprivation on the first day of
954 handling (Day 1). Mice were handled for 2 days (twice per day for 2 minutes, Days 1-2).
955 On Day 2, after the second handling session, mice underwent one 10-minute
956 habituation session in which they were exposed to the experimental apparatus in the
957 presence of cheerios spread across the chamber to encourage exploration (no saucers
958 present). Starting on the day after habituation (Day 3), mice underwent two days of
959 training to dig (6 trials/day), when they learn to dig in the saucer filled with bed-o-cob
960 bedding for a cheerio reward. The bedding amount was increased incrementally over
961 the six daily sessions until the cheerio was fully covered. On the following day (Day 5),
962 animals underwent rule acquisition. During rule acquisition, animals were exposed to
963 two saucers displaying a pseudorandom, counterbalanced combination of one of the
964 two beddings and scents, one of which contained a cheerio reward. The reward was
965 paired with one of the scents (rule; counterbalanced) for the first five warm-up trials until
966 they found the cheerio. From trial six onwards, once the animal's snout crossed the
967 edge of the saucer, this was considered a decision, which was followed by enclosing
968 the animal within the side of the chamber for 30 seconds using a sliding door. Trials ran
969 until animals reached the criterion of 8 correct choices within 10 consecutive trials,
970 taken as a proxy for learning the scent–reward association. The next day (Day 6), mice
971 underwent extradimensional (ED) set shifting. During ED set shifting, a similar

972 procedure from rule acquisition was followed, but the bedding medium (instead of the
973 scent) predicted the cheerio location. Trials ran until animals reached the criterion of 8
974 correct choices within 10 consecutive trials. Animals that did not meet this criterion
975 before reaching 70 trials were excluded from the experiment. Scent and bedding types
976 were counterbalanced between animals. Trials were recorded using the Imaging Source
977 DMK 22AUC03 1.1.3 IR camera and distance travelled and time to first choice were
978 quantified using ANYmaze software (Stoelting, USA). Trials to criterion were quantified
979 manually by a blind experimenter and validated through ANYmaze. Two juvenile hM4D
980 animals showed an outlier profile for distance travelled during set shifting (3.78m and
981 3.98m), which was solely driven by exploration after choice (while eating the food
982 reward) and were therefore excluded from that analysis.

983 Quantification and statistical analysis

984 Data are presented as mean ± SEM with n shown as the number of animals for
985 histological experiments, or number of cells followed by number of animals in
986 parenthesis for electrophysiological experiments. Due to space limits, only significant p
987 is reported in the main text, with all other detailed statistical analyses (including sex
988 differences and nested ANOVAS) reported in Table S1. All statistical analyses were
989 performed in GraphPad Prism® version 9 or Jamovi version 2.7.6 software through one-
990 way ANOVA, two-way repeated-measures or nested ANOVAs, where appropriate.
991 Omnibus test results (F values) are reported in Table S1. To test for group differences
992 following ANOVA, we applied the software default of Tukey's, Bonferroni's or Šídák's-
993 corrected post hoc tests for all pairwise comparisons following non-repeated and
994 repeated measures ANOVA, respectively, and significant results were denoted by

995 asterisks in associated figures. Potential sex differences were first assessed using a
996 two-way, repeated measures ANOVA and in the absence of effects, data were
997 collapsed across these variables for subsequent analyses. Outliers were detected using
998 the software outlier test (Grubbs' Test or the extreme studentized deviant method) and
999 removed from the dataset prior to running group and/or post hoc comparisons.

1000

1001 KEY RESOURCES TABLE

REAGENT or RESOURCE	SOURCE	IDENTIFIER
Antibodies		
Monoclonal rat anti-mCherry (#M11217)	ThermoFisher	RRID: AB_2536611
Polyclonal rabbit anti-cFos (#226 003)	Synaptic Systems	RRID: AB_2231974
Goat anti-rat Alexa 568 (#A11077)	ThermoFisher	RRID: AB_2534121
Donkey anti-rabbit horseradish peroxidase (#711-036-152)	Jackson ImmunoResearch	RRID: AB_2340590
Polyclonal chicken anti-GFP (#AB13970)	Abcam	RRID: AB_300798
Goat anti-chicken Alexa 488 (#A11039)	Invitrogen	RRID: AB_2534096
Hoechst 33342 nuclear dye (#H1399)	ThermoFisher	
Bacterial and virus strains		
AAV1-CaMKIIa-hChR2(H134R)-EYFP	Addgene	# 26969-AAV1
Red RetroBeads	LumaFluor Inc	R170
pENN-AAV-hSyn-Cre-WPRE-hGH (Retrograde)	Addgene	#105553-AAVrg
pAAV5-hSyn-DIO-hM4D(Gi)-mCherry	Addgene	#44362-AAV5
pAAV5-hSyn-DIO-mCherry	Addgene	#50459-AAV5
Experimental models: Organism/strains		
Mouse: C57BL/6J	The Jackson Laboratory	
Chemicals, peptides, and recombinant proteins		
Ketamine (Narketan 100 mg/mL Vial/10 ml)	CDMV	#032N
Xylazine (AnaSed 100 mg/mL Btle/ 50ml)	CDMV	#113537

Avertin (2% 2,2,2-tribromoethanol + tert-amyl alcohol in 0.1M PBS)	Sigma-Aldrich	#T48402 #240486
Tetrodotoxin citrate, Na+ channel blocker, 1mg (TTX)	HelloBio	#HB1035
4-Aminopyridine, K+ channel blocker, 100mg (4-AP)	Abcam	#AB120122
Compund-21, water soluble (C21)	HelloBio	#HB6124
Software		
ImageJ/Fiji	NIH, MD, USA	https://imagej.net /software/fiji/
ANYmaze	Stoelting Company	#60605
MiniAnalysis (Synaptosoft)		

1002

1003

1004

1005 **Supplemental Figures and Legends:**

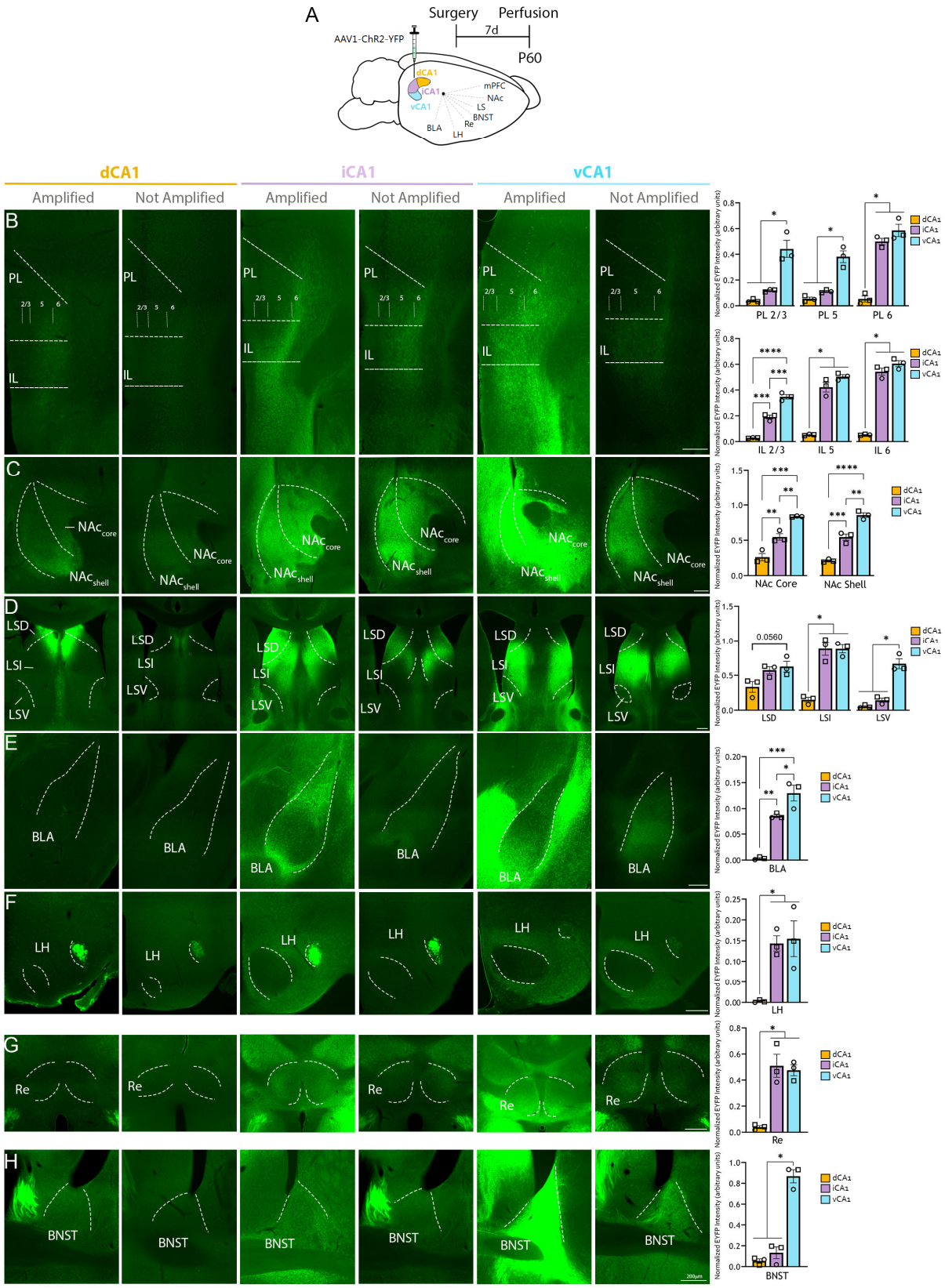
A
Surgery
Perfusion
7d
P60
AAV1-ChR2-YFP
dCA1
iCA1
vCA1
mPFC
NAc
LS
BNST
Re
LH
BLA
dCA1
iCA1
vCA1
Amplified
Not Amplified
B
PL
IL
C
NAc core
NAc shell
D
LSD
LSI
LSV
E
BLA
F
LH
G
Re
H
BNST
Normalized EYFP Intensity (arbitrary units)
PL 2/3
PL 5
PL 6
IL 2/3
IL 5
IL 6
NAc Core
NAc Shell
LSD
LSI
LSV
BLA
LH
Re
BNST

1007 **Figure S1. Comparison of projection patterns from dorsal, intermediate and**
1008 **ventral CA1 in adult mice. A**. C57BL/6J mice were injected with AAV-ChR2-YFP virus
1009 in the dorsal, intermediate or ventral CA1 and perfused seven days later at P60 for
1010 tissue and image processing. **B-H.** Example images and quantification of differences
1011 between projections from dCA1 (left image columns) and those from intermediate iCA1
1012 (middle image columns) and vCA1 (right most columns), with the iCA1 and vCA1
1013 projections showing largely similar patterns across examined regions. The left most
1014 column of each CA1 set of images (dCA1 amplified, iCA1 amplified, vCA1 amplified)
1015 underwent immunohistochemistry against GFP to amplify viral signal. All other (not
1016 amplified) images show direct fluorescence under identical settings. Graphs on the right
1017 show semi-quantification of terminal density of amplified images for each of the three
1018 pathways across all regions. BNST = bed nucleus of the stria terminalis, BLA =
1019 basolateral amygdala, IL = infralimbic cortex, LH = lateral hypothalamus, LSD = dorsal
1020 lateral septum, LSI = intermediate lateral septum, LSV = ventral lateral septum; NAc =
1021 nucleus accumbens, PL= prelimbic cortex, Re = thalamic nucleus reuniens. Scale bar:
1022 200μm. n=3 per projection. Individual female datapoints represented as circles, male as
1023 squares. *p<0.05, **p<0.01, ***p<0.001, ****p<0.0001.

1024

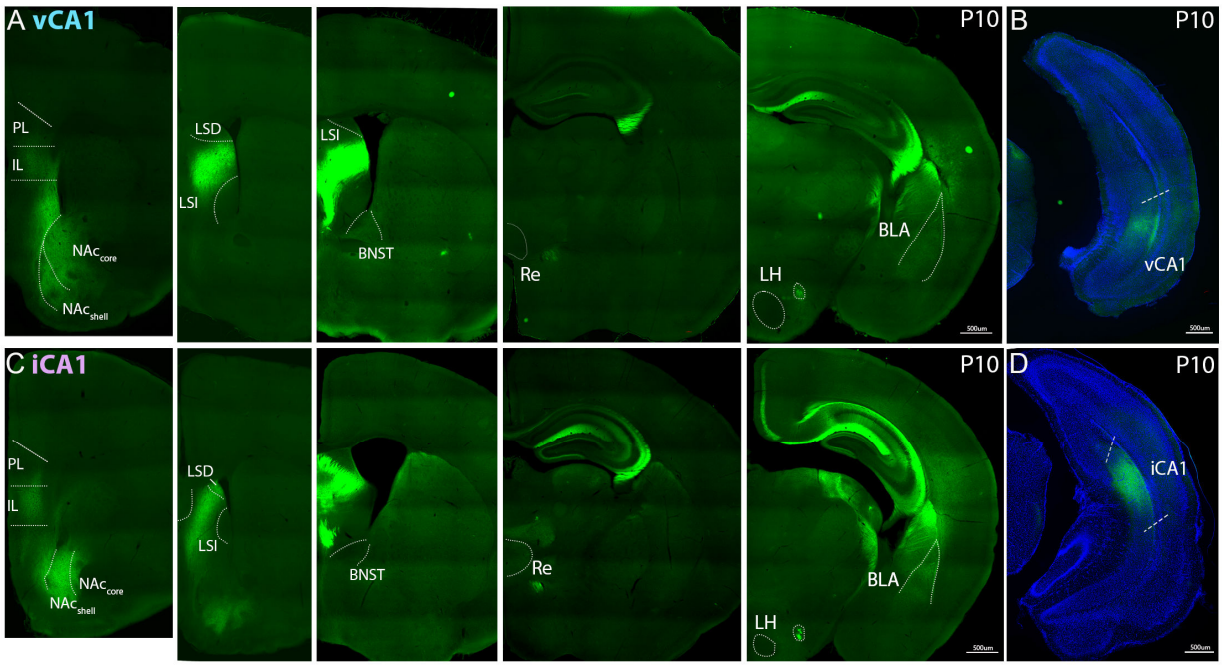

1025

1026 **Figure S2. iCA1 and vCA1 axons are already present in all target areas by P10.**
1027 C57BL/6J mice were injected with AAV-ChR2-YFP virus in the ventral (vCA1; **A-B**) or
1028 intermediate (iCA1; **C-D**) CA1 at P3 and perfused seven days later at P10 for tissue and
1029 image processing. **A** and **C** show terminal projections for each pathway (**A**: vCA1; **C**:
1030 iCA1), whereas **B** and **D** show viral expression at the respective infusion site. vCA1 and

1031 iCA1 axons were already visible at P10 in the prelimbic cortex (PL), infralimbic cortex
1032 (IL), nucleus accumbens (NAc) core and shell, dorsal lateral septum (LSD) and
1033 intermediate lateral septum (LSI), thalamic nucleus reuniens (Re), basolateral amygdala
1034 (BLA), bed nucleus of the stria terminalis (BNST), and lateral hypothalamus (LH). Scale
1035 bar: 500μm.

1036

1037

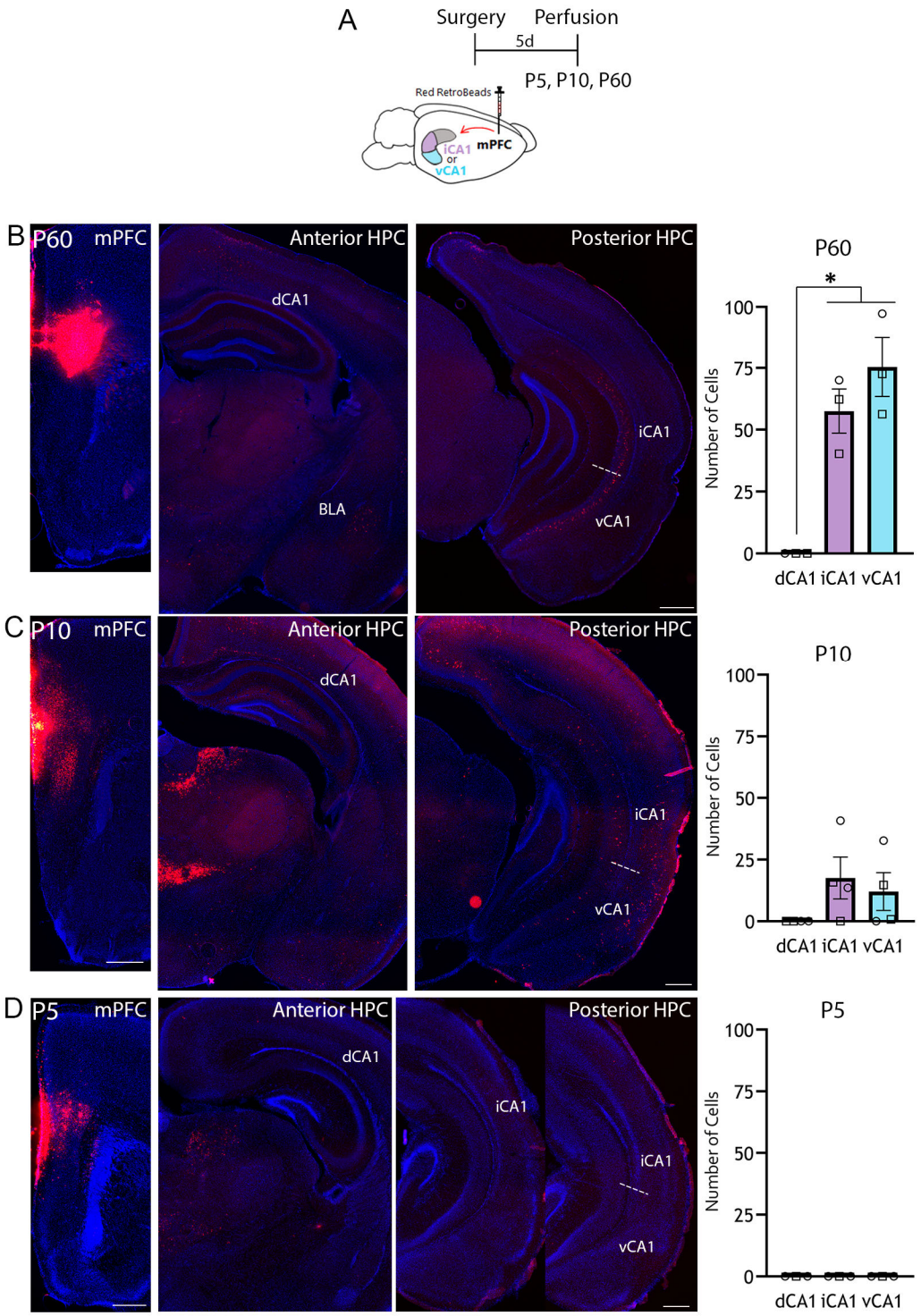

Figure S3. CA1 terminals arrive at the mPFC between P0 and P10 in C57BL/6J mice. A. Schematic of experiment. C57BL/6J mice were infused with red Lumafluor RetroBeads™ unilaterally at the medial prefrontal cortex (mPFC). Mice were transcardially perfused 5 days following surgery at P5, P10 or P60. **B**. Sample image of the mPFC infusion site in an adult P60 brain (*left most image*) shows absence of red

1044 soma signal at the dorsal CA1 (dCA1) but labeled cells in the basolateral amygdala
1045 (BLA) (*center image*) and in the intermediate CA1 (iCA1) and ventral CA1 (vCA1) (*right*
1046 *most image*). **C**. Sample image of the mPFC infusion site in a P10 brain (*left most*
1047 *image*) showing absence of red soma signal at the dCA1 but labeled cells in the BLA
1048 (*center image*), as well as in the iCA1 and vCA1 (*right most image*). **D**. Sample image of
1049 the mPFC infusion site in a P5 brain (*left most image*) showing absence of red soma
1050 signal at the dCA1, iCA1 or vCA1 (*right most images*). Graphs on the right show
1051 quantification of the number of labeled cells in the dCA1, iCA1 and vCA1. n=3 for each
1052 age. Individual female datapoints represented as circles, male as squares. *$p<0.05$.
1053 Scale bar: 500μm.

1054

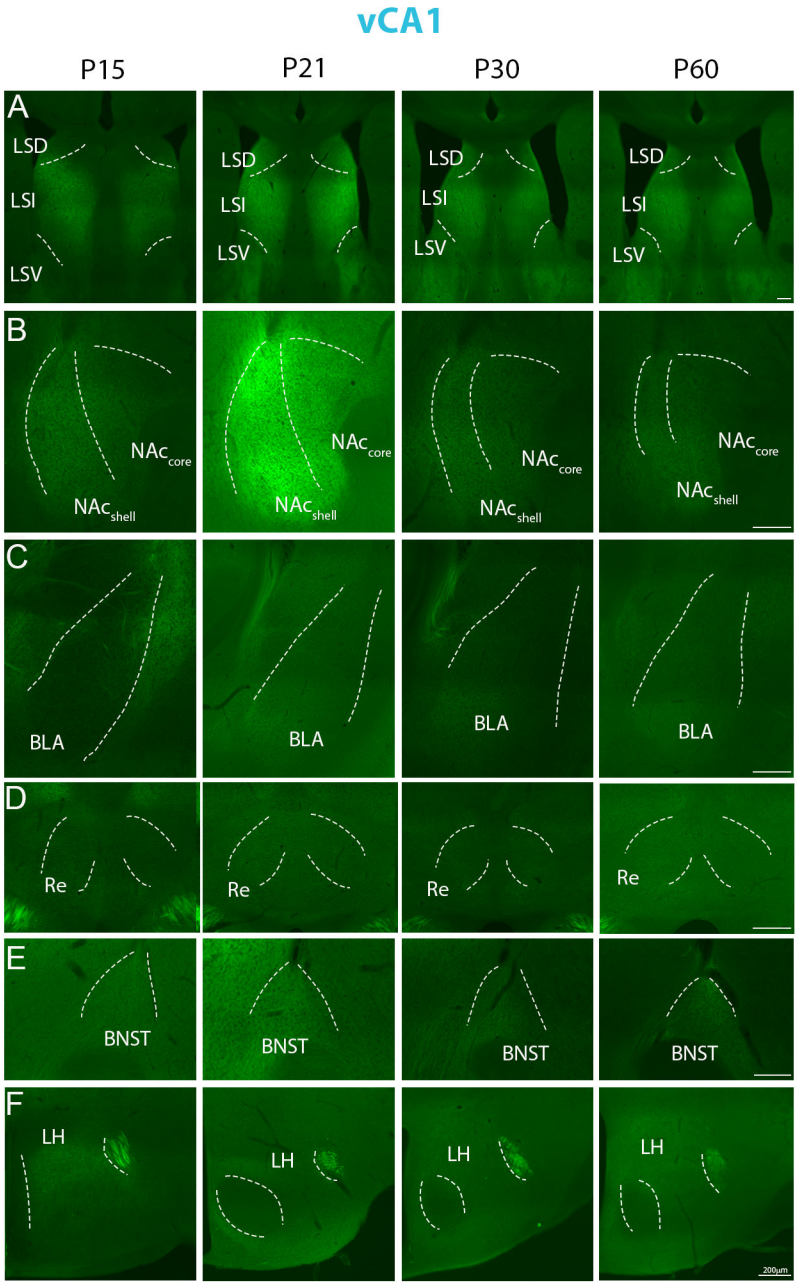

Figure S4. Example images showing developmental changes in vCA1 terminal density. C57BL/6J mice were injected with AAV-ChR2-YFP virus in the vCA1 and perfused seven days later at P15, P21, P30 or P60 for tissue and image processing. Images show vCA1 terminal expression across ages in the dorsal lateral septum (LSD; **A**), ventral lateral septum (LSV; **A**), intermediate lateral septum (LSI; **A**), nucleus accumbens (NAc) core (**B**) and shell (**B**); basolateral amygdala (BLA; **C**), thalamic nucleus reuniens (Re; **D**), bed nucleus of the stria terminalis (BNST; **E**), and lateral hypothalamus (LH; **F**).

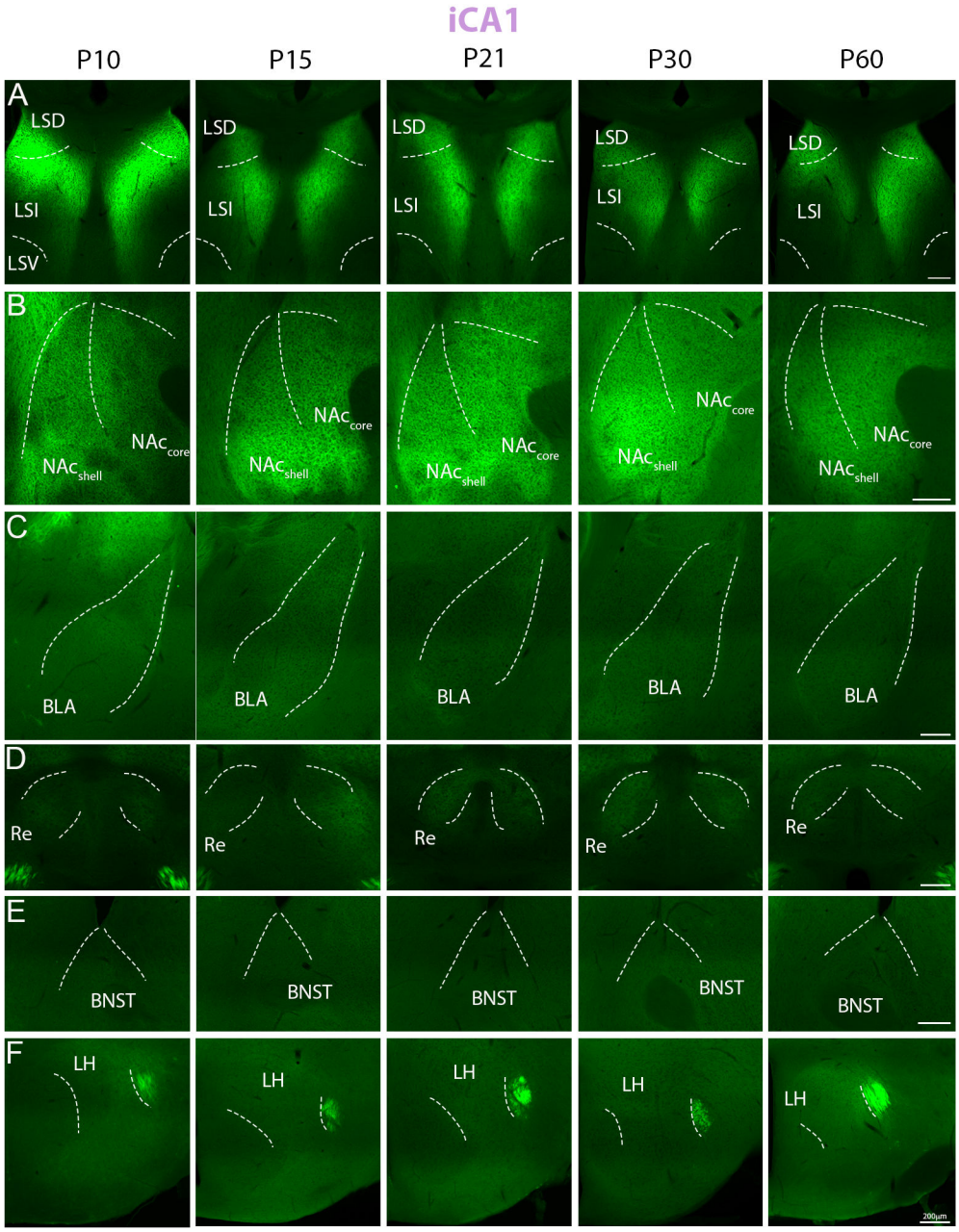

1065

1066 **Figure S5. Example images showing developmental changes in iCA1 terminal**
1067 **density.** C57BL/6J mice were injected with AAV-ChR2-YFP virus in the iCA1 and
1068 perfused seven days later at P10, P15, P21, P30 or P60 for tissue and image
1069 processing. Images show iCA1 terminal expression across ages in the dorsal lateral
1070 septum (LSD; **A**), intermediate lateral septum (LSI; **A**), nucleus accumbens (NAc) core
1071 (**B**) and shell (**B**); basolateral amygdala (BLA; **C**), thalamic nucleus reuniens (Re; **D**),
1072 bed nucleus of the stria terminalis (BNST; **E**), and lateral hypothalamus (LH; **F**). LSV =
1073 ventral lateral septum.

1074

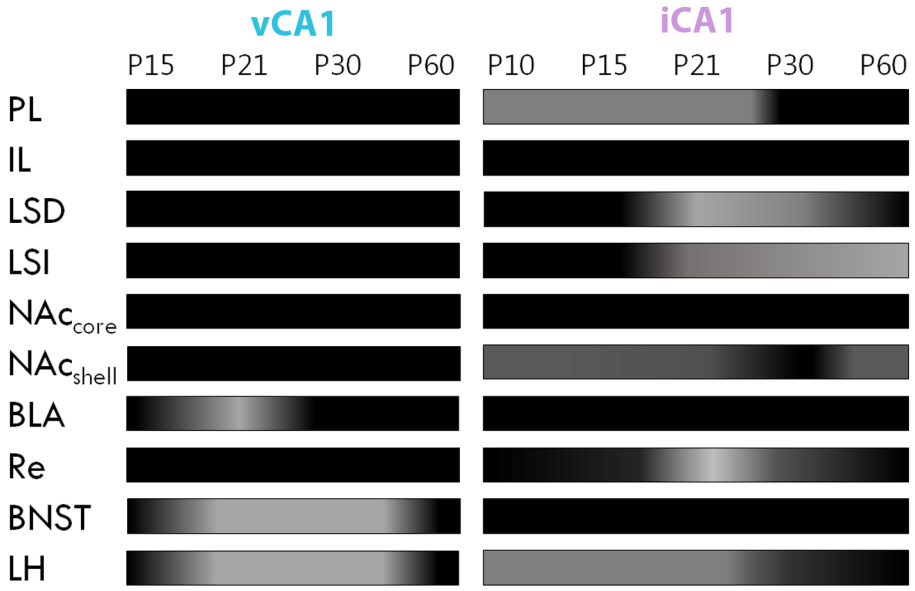

Figure S6. Graphic representation of anatomical maturation data for vCA1 and iCA1 projections. Rectangular heatmaps represent relative changes in terminal density across respective ages, whereby darker color represents an increase. PL = prelimbic cortex, IL = infralimbic cortex, NAc = nucleus accumbens, LSD = dorsal lateral septum, LSI = intermediate lateral septum, Re = thalamic nucleus reuniens, BLA = basolateral amygdala, BNST = bed nucleus of the stria terminalis, LH = lateral hypothalamus.

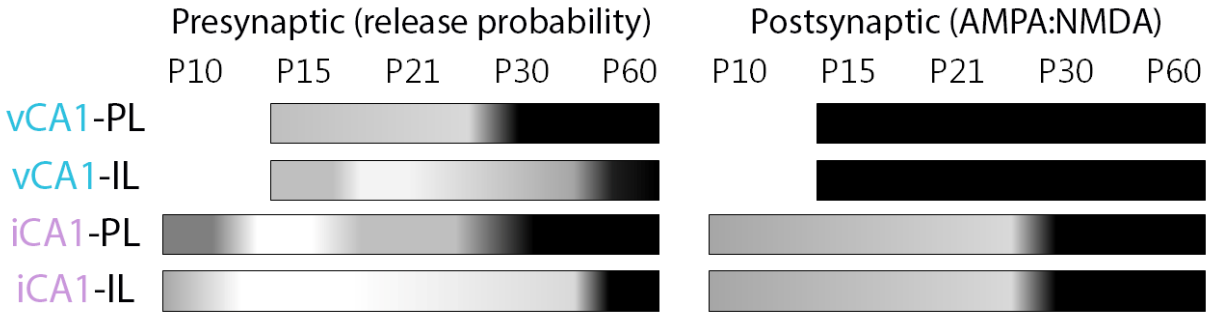

Figure S7. Graphic representation of evoked synaptic maturation data for vCA1- and iCA1- PL and IL pathways. Rectangular heatmaps represent relative changes in presynaptic (**Left**; or release probability, the inverted function of the paired pulse ratios) and postsynaptic efficacy (**Right**, represented as AMPA:NMDA ratios) across respective ages, whereby darker color represents an increase. PL = prelimbic cortex, IL = infralimbic cortex.

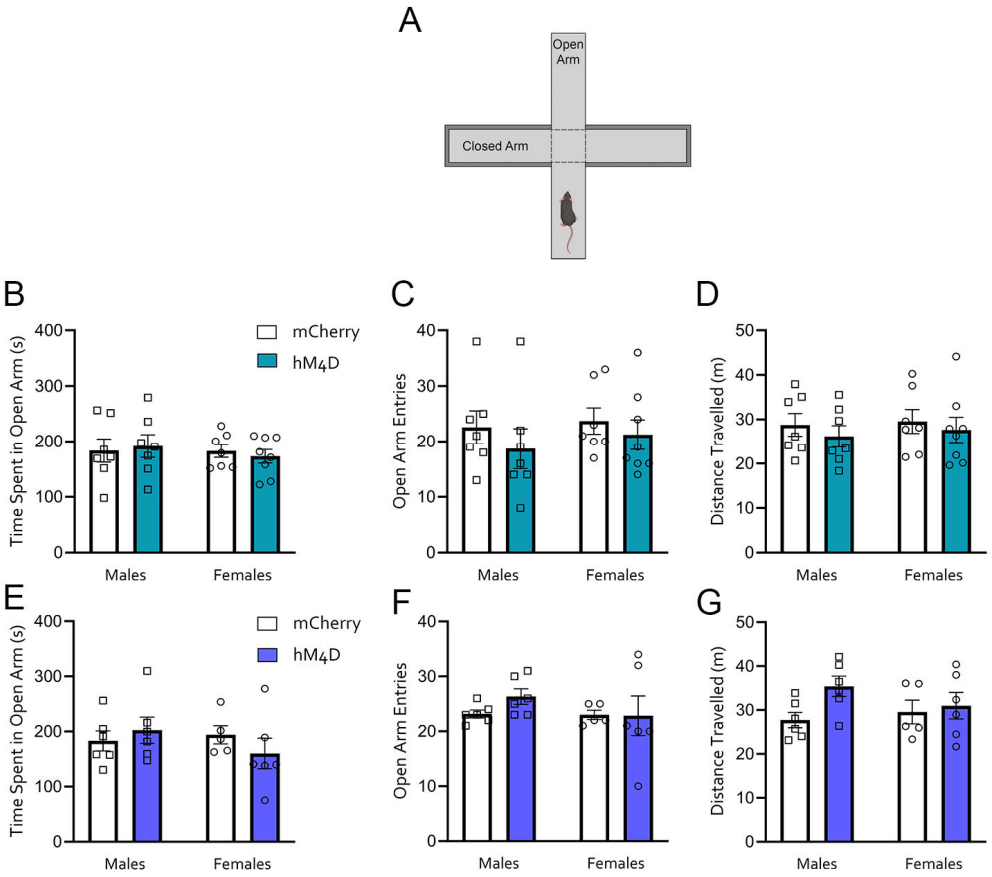

1091

1092 **Figure S8. Chronic inhibition of the vCA1-mPFC pathway does not affect long-**
1093 **term performance in the elevated plus maze. A.** Following the experiments from
1094 Figure 6, animals in both the juvenile and adult cohorts were tested in the elevated plus
1095 maze (EPM) in the absence of C21. **B-D**. Juvenile cohort. mCherry and hM4D animals
1096 that underwent C21 treatment from P15-P30 did not differ in time spent in the open
1097 arms of the EPM (**B**), number of open arm entries (**C**) or distance travelled (**D**). mCherry
1098 n= 14 (7 females, 7 males); hM4D n= 15 (8 females, 7 males). **E-G**. Adult cohort.
1099 mCherry and hM4D animals that underwent C21 treatment from P60-P75 showed
1100 equivalent time spent in the open arms of the EPM (**E**), number of open arm entries (**F**)
1101 or distance travelled (**G**). mCherry n= 11 (5 females, 6 males); hM4D n= 12 (6 females,
1102 6 males). Individual female datapoints are represented as circles, and males as
1103 squares.

1104

1105 **References:**

1106 1. Eichenbaum, H. Hippocampus : Cognitive Processes and Neural Representations
1107 that Underlie Declarative Memory The hippocampus serves a critical role in
1108 declarative. *Neuron* **44**, 109–120 (2004).

1109 2. O'Keefe, J. & Nadel, L. *The Hippocampus as a Cognitive Map*. *Hippocampus*

1110 (1978).

1111 3. Kheirbek, M. a *et al.* Differential control of learning and anxiety along the
1112 dorsoventral axis of the dentate gyrus. *Neuron* **77**, 955–68 (2013).

1113 4. Jimenez, J. C. *et al.* Anxiety Cells in a Hippocampal-Hypothalamic Circuit. *Neuron*
1114 **97**, 670–683 (2018).

1115 5. Gray, J. & Mcnaughton, N. *The Neuropsychology of Anxiety : An enquiry into the*
1116 *function of the septo- hippocampal system Abstract and Keywords*. (2003).
1117 doi:10.1093/acprof.

1118 6. Fanselow, M. S. & Dong, H.-W. Are the dorsal and ventral hippocampus
1119 functionally distinct structures? *Neuron* **65**, 7–19 (2010).

1120 7. Besnard, A., Miller, S. M. & Sahay, A. Distinct Dorsal and Ventral Hippocampal
1121 CA3 Outputs Govern Contextual Fear Discrimination. *Cell Rep.* **30**, 2360-2373.e5
1122 (2020).

1123 8. Sheehan, T. P., Chambers, R. A. & Russell, D. S. Regulation of affect by the
1124 lateral septum: Implications for neuropsychiatry. *Brain Res. Rev.* **46**, 71–117
1125 (2004).

1126 9. AlSubaie, R. *et al.* Control of Parallel Hippocampal Output Pathways by
1127 Amygdalar Long-Range Inhibition. *bioRxiv* 2021.03.08.434367 (2021).

1128 10. Griffin, A. L. Role of the thalamic nucleus reunions in mediating interactions
1129 between the hippocampus and medial prefrontal cortex during spatial working
1130 memory. *Front. Syst. Neurosci.* **9**, 1–8 (2015).

1131 11. Eichenbaum, H. Prefrontal–hippocampal interactions in episodic memory. *Nat.*
1132 *Rev. Neurosci.* **18**, 547–558 (2017).

1133 12. Jin, J. & Maren, S. Prefrontal-hippocampal interactions in memory and emotion.
1134 *Front. Syst. Neurosci.* **9**, 1–8 (2015).

1135 13. Sweeney, P. & Yang, Y. An inhibitory septum to lateral hypothalamus circuit that
1136 suppresses feeding. *J. Neurosci.* **36**, 11185–11195 (2016).

1137 14. Strange, B. A., Witter, M. P., Lein, E. S. & Moser, E. I. Functional organization of
1138 the hippocampal longitudinal axis. *Nat. Rev. Neurosci.* **15**, 655–669 (2014).

1139 15. Amaral, D. G. & Witter, M. P. The three-dimensional organization of the
1140 hippocampal formation: a review of anatomical data. *Neuroscience* **31**, 571–591
1141 (1989).

1142 16. Moser, M. B. & Moser, E. I. Functional differentiation in the hippocampus.
1143 *Hippocampus* **8**, 608–619 (1998).

1144 17. Cembrowski, M. S. *et al.* Spatial Gene-Expression Gradients Underlie Prominent
1145 Heterogeneity of CA1 Pyramidal Neurons. *Neuron* **89**, 351–368 (2016).

1146 18. Thompson, C. L. *et al.* Genomic Anatomy of the Hippocampus. *Neuron* **60**, 1010–
1147 1021 (2008).

1148 19. Malik, R., Dougherty, K. A., Parikh, K., Byrne, C. & Johnston, D. Mapping the
1149 Electrophysiological and Morphological Properties of CA1 Pyramidal Neurons
1150 Along the Longitudinal Hippocampal Axis. **361**, 341–361 (2016).

1151 20. Jinno, S., Aika, Y., Fukuda, T. & Kosaka, T. Quantitative Analysis of Neuronal
1152 Nitric Oxide Synthase-Immunoreactive Neurons in the Mouse Hippocampus With
1153 Optical Disector. **412**, 398–412 (1999).

1154 21. Milior, G. *et al.* Electrophysiological Properties of CA1 Pyramidal Neurons along
1155 the Longitudinal Axis of the Mouse Hippocampus. *Nat. Publ. Gr.* 1–9 (2016)
1156 doi:10.1038/srep38242.

1157 22. Dong, H. W., Swanson, L. W., Chen, L., Fanselow, M. S. & Toga, A. W. Genomic-
1158 anatomic evidence for distinct functional domains in hippocampal field CA1. *Proc.*
1159 *Natl. Acad. Sci. U. S. A.* **106**, 11794–11799 (2009).

1160 23. Fanselow, M. S. & Dong, H. W. Are the Dorsal and Ventral Hippocampus
1161 Functionally Distinct Structures? *Neuron* **65**, 7–19 (2010).

1162 24. Biane, J. S. *et al.* Neural dynamics underlying associative learning in the dorsal
1163 and ventral hippocampus. *Nat. Neurosci.* **26**, 798–809 (2023).

1164 25. Jarzebowski, P., Hay, Y. A., Grewe, B. F. & Paulsen, O. Different encoding of
1165 reward location in dorsal and intermediate hippocampus. *Curr. Biol.* **32**, 834-
1166 841.e5 (2022).

1167 26. Barker, G. R. I. *et al.* Separate elements of episodic memory subserved by
1168 distinct hippocampal – prefrontal connections. *Nat. Neurosci.* **20**, (2017).

1169 27. Kheirbek, M. A. *et al.* Differential control of learning and anxiety along the
1170 dorsoventral axis of the dentate gyrus. *Neuron* **77**, 955–968 (2013).

1171 28. Bannerman, D. M. *et al.* Regional dissociations within the hippocampus - Memory
1172 and anxiety. *Neuroscience and Biobehavioral Reviews* (2004)
1173 doi:10.1016/j.neubiorev.2004.03.004.

1174 29. Bast, T., Wilson, L. A., Witter, M. P. & Morris, R. G. M. From rapid place learning
1175 to behavioral performance: A key role for the intermediate hippocampus. *PLoS*
1176 *Biol.* **7**, 0730–0746 (2009).

1177 30. Barker, G. R. I. *et al.* Separate elements of episodic memory subserved by
1178 distinct hippocampal-prefrontal connections. *Nat. Neurosci.* **20**, 242–250 (2017).

1179 31. O'Reilly, K. C. *et al.* Identification of dorsal–ventral hippocampal differentiation in
1180 neonatal rats. *Brain Struct. Funct.* **220**, 2873–2893 (2015).

1181 32. Lee, A. R., Kim, J. H., Cho, E., Kim, M. & Park, M. Dorsal and ventral
1182 hippocampus differentiate in functional pathways and differentially associate with
1183 neurological disease-related genes during postnatal development. *Front. Mol.*
1184 *Neurosci.* **10**, 1–14 (2017).

1185 33. Paus, T., Keshavan, M. & Giedd, J. N. Why do many psychiatric disorders
1186 emerge during adolescence? *Nat. Rev. Neurosci.* **9**, 947–957 (2008).

1187 34. Lee, F. S. *et al.* Adolescent mental health— Opportunity and obligation. *Science*
1188 *(80-.).* **346**, 547–549 (2014).

1189 35. Casey, B. J., Glatt, C. E. & Lee, F. S. Treating the Developing versus Developed
1190 Brain: Translating Preclinical Mouse and Human Studies. *Neuron* **86**, 1358–1368
1191 (2015).

1192 36. Manoach, D. S. Prefrontal cortex dysfunction during working memory
1193 performance in schizophrenia: Reconciling discrepant findings. *Schizophr. Res.*
1194 **60**, 285–298 (2003).

1195 37. Berman, K. F. & Weinberger, D. R. Chapter 26 The prefrontal cortex in
1196 schizophrenia and other neuropsychiatric diseases: In vivo physiological
1197 correlates of cognitive deficits. *Prog. Brain Res.* **85**, 521–537 (1991).

1198 38. Meyer-Lindenberg, A. S. *et al.* Regionally specific disturbance of dorsolateral
1199 prefrontal-hippocampal functional connectivity in schizophrenia. *Arch. Gen.*
1200 *Psychiatry* **62**, 379–386 (2005).

1201 39. Wolf, R. C. *et al.* Temporally anticorrelated brain networks during working memory
1202 performance reveal aberrant prefrontal and hippocampal connectivity in patients
1203 with schizophrenia. *Prog. Neuro-Psychopharmacology Biol. Psychiatry* **33**, 1464–
1204 1473 (2009).

1205 40. Sigurdsson, T., Stark, K. L., Karayiorgou, M., Gogos, J. A. & Gordon, J. A.
1206 Impaired hippocampal-prefrontal synchrony in a genetic mouse model of
1207 schizophrenia. *Nature* **464**, 763–767 (2010).

1208 41. Bogerts, B. Recent advances in defining the neuropathology of schizophrenia.
1209 *Acta Neuropathol.* **19**, 431–445 (1993).

1210 42. MacMaster, F. P. & Kusumakar, V. Hippocampal volume in early onset
1211 depression. *BMC Med.* **2**, 2 (2004).

1212 43. Rao, U. *et al.* Hippocampal changes associated with early-life adversity and
1213 vulnerability to depression. *Biol. Psychiatry* **67**, 357–64 (2010).

1214 44. Sigurdsson, T. & Duvarci, S. Hippocampal-Prefrontal Interactions in Cognition ,
1215 Behavior and Psychiatric Disease. **9**, 1–18 (2016).

1216 45. Li, M., Long, C. & Yang, L. Hippocampal-prefrontal circuit and disrupted functional
1217 connectivity in psychiatric and neurodegenerative disorders. *Biomed Res. Int.*
1218 **2015**, (2015).

1219 46. Hartung, H. *et al.* From Shortage to Surge: A Developmental Switch in
1220 Hippocampal-Prefrontal Coupling in a Gene-Environment Model of
1221 Neuropsychiatric Disorders. *Cereb. Cortex* **26**, 4265–4281 (2016).

1222 47. Oberlander, V. C., Xu, X., Chini, M. & Hanganu-Opatz, I. L. Developmental
1223 dysfunction of prefrontal–hippocampal networks in mouse models of mental
1224 illness. *Eur. J. Neurosci.* **50**, 3072–3084 (2019).

1225 48. Xu, X., Song, L. & Hanganu-Opatz, I. L. Knock-Down of Hippocampal DISC1 in
1226 Immune-Challenged Mice Impairs the Prefrontal-Hippocampal Coupling and the
1227 Cognitive Performance throughout Development. *Cereb. Cortex* **31**, 1240–1258
1228 (2021).

1229 49. Zerbi, V. *et al.* Dysfunctional autism risk genes cause circuit-specific connectivity
1230 deficits with distinct developmental trajectories. *Cereb. Cortex* **28**, 2495–2506
1231 (2018).

1232 50. Tamura, M., Mukai, J., Gordon, J. A. & Gogos, J. A. Developmental Inhibition of
1233 Gsk3 Rescues Behavioral and Neurophysiological Deficits in a Mouse Model of
1234 Schizophrenia Predisposition. *Neuron* **89**, 1100–1109 (2016).

1235 51. Chini, M. & Hanganu-Opatz, I. L. Prefrontal Cortex Development in Health and
1236 Disease: Lessons from Rodents and Humans. *Trends Neurosci.* **44**, 227–240
1237 (2021).

1238 52. Barón-Mendoza, I. *et al.* Dendritic complexity in prefrontal cortex and
1239 hippocampus of the autistic-like mice C58/J. *Neurosci. Lett.* **703**, 149–155 (2019).

1240 53. Adams, R. A. *et al.* Impaired theta phase coupling underlies frontotemporal
1241 dysconnectivity in schizophrenia. *Brain* **143**, 1261–1277 (2020).

1242 54. Cenquizca, L. A. & Swanson, L. W. Spatial organization of direct hippocampal
1243 field CA1 axonal projections to the rest of the cerebral cortex. *Brain Res. Rev.* **56**,
1244 1–26 (2007).

1245 55. Ahlbeck, J., Song, L., Chini, M., Bitzenhofer, S. H. & Hanganu-Opatz, I. L.
1246 Glutamatergic drive along the septotemporal axis of hippocampus boosts
1247 prelimbic oscillations in the neonatal mouse. *Elife* **7**, 1–24 (2018).

1248 56. Takita, M., Fujiwara, S. E. & Izaki, Y. Functional structure of the intermediate and
1249 ventral hippocampo-prefrontal pathway in the prefrontal convergent system. *J.*

1250 *Physiol. Paris* **107**, 441–447 (2013).

1251 57. Little, J. P. & Carter, A. G. Subcellular Synaptic Connectivity of Layer 2 Pyramidal
1252 Neurons in the Medial Prefrontal Cortex. *J. Neurosci.* **32**, 12808–12819 (2012).

1253 58. Liu, X. & Carter, A. G. Ventral Hippocampal Inputs Preferentially Drive
1254 Corticocortical Neurons in the Infralimbic Prefrontal Cortex. **38**, 7351–7363
1255 (2018).

1256 59. Hallock, H. L. *et al.* Molecularly-Defined Hippocampal Inputs Regulate Population
1257 Dynamics in the Prelimbic Cortex to Suppress Context Fear Memory Retrieval.
1258 *Biol. Psychiatry* 802967 (2020) doi:10.1016/j.biopsych.2020.04.014.

1259 60. Lee, A. T. *et al.* VIP Interneurons Contribute to Avoidance Behavior by Regulating
1260 Information Flow across Hippocampal-Prefrontal Networks. *Neuron* **102**, 1223-
1261 1234.e4 (2019).

1262 61. Schlichting, M. L., Preston, A. R., States, U., States, U. & States, U. HHS Public
1263 Access. 1–8 (2016) doi:10.1016/j.cobeha.2014.07.005.Memory.

1264 62. Sánchez-Bellot, C., AlSubaie, R., Mishchanchuk, K., Wee, R. W. S. & MacAskill,
1265 A. F. Two opposing hippocampus to prefrontal cortex pathways for the control of
1266 approach and avoidance behaviour. *Nat. Commun.* **13**, 1–17 (2022).

1267 63. Williams, S. A. *et al.* Hippocampal Disinhibition Reduces Contextual and
1268 Elemental Fear Conditioning While Sparing the Acquisition of Latent Inhibition.
1269 *eNeuro* **9**, 1–14 (2022).

1270 64. Labouesse, M. A., Langhans, W. & Meyer, U. Abnormal context–reward
1271 associations in an immune-mediated neurodevelopmental mouse model with
1272 relevance to schizophrenia. *Transl. Psychiatry* **5**, 1–9 (2015).

1273 65. Hensch, T. K. Critical period regulation. *Annu. Rev. Neurosci.* **27**, 549–579
1274 (2004).

1275 66. Fox, K. A Critical Period for Experience-dependent Barrel Cortex Synaptic
1276 Plasticity in Rat. *J. Neurosci.* **12**, 1626–1636 (1992).

1277 67. Fagiolini, M., Pizzorusso, T., Berardi, N., Domenici, L. & Maffei, L. Functional
1278 postnatal development of the rat primary visual cortex and the role of visual
1279 experience: dark rearing and monocular deprivation. *Vision Res.* **34**, 709–20
1280 (1994).

1281 68. Gordon, A. & Sttyker, P. Experience-Dependent Primary Visual Cortex Plasticity
1282 of Binocular of the Mouse Responses in the. **76**, 3274–3286 (1996).

1283 69. Travaglia, A., Steinmetz, A. B., Miranda, J. M. & Alberini, C. M. Mechanisms of
1284 critical period in the hippocampus underlie object location learning and memory in

1285 infant rats. *Learn. Mem.* **25**, 176–182 (2018).

1286 70. Alberini, C. M. & Travaglia, A. Infantile amnesia: A critical period of learning to
1287 learn and remember. *J. Neurosci.* **37**, 5783–5795 (2017).

1288 71. Ramsaran, A. I., Schlichting, M. L. & Frankland, P. W. The ontogeny of memory
1289 persistence and specificity. *Dev. Cogn. Neurosci.* **36**, 100591 (2019).

1290 72. Thomases, D. R., Cass, D. K. & Tseng, K. Y. Periadolescent exposure to the
1291 NMDA receptor antagonist MK-801 impairs the functional maturation of local
1292 GABAergic circuits in the adult prefrontal cortex. *J. Neurosci.* **33**, 26–34 (2013).

1293 73. Rebello, T. J. *et al.* Postnatal Day 2 to 11 Constitutes a 5-HT-Sensitive Period
1294 Impacting Adult mPFC Function. *J. Neurosci.* **34**, 12379–12393 (2014).

1295 74. Callaghan, B. L., Graham, B. M., Li, S. & Richardson, R. From resilience to
1296 vulnerability: Mechanistic insights into the effects of stress on transitions in critical
1297 period plasticity. *Front. Psychiatry* **4**, 1–15 (2013).

1298 75. Nabel, E. M. & Morishita, H. Regulating critical period plasticity: Insight from the
1299 visual system to fear circuitry for therapeutic interventions. *Front. Psychiatry* **4**, 1–
1300 8 (2013).

1301 76. Klune, C. B., Jin, B. & DeNardo, L. A. Linking mPFC circuit maturation to the
1302 developmental regulation of emotional memory and cognitive flexibility. *Elife* **10**,
1303 (2021).

1304 77. Espinosa, J. S. & Stryker, M. P. Development and Plasticity of the Primary Visual
1305 Cortex. *Neuron* **75**, 230–249 (2012).

1306 78. Hubel, D. & Wiesel, T. THE PERIOD OF SUSCEPTIBILITY TO THE
1307 PHYSIOLOGICAL EFFECTS OF UNILATERAL EYE CLOSURE IN KITTENS. *J.*
1308 *Physiol.* **206**, 419–436 (1970).

1309 79. Erzurumlu, R. S. & Gaspar, P. Development and critical period plasticity of the
1310 barrel cortex. *Eur. J. Neurosci.* **35**, 1540–1553 (2012).

1311 80. Perica, M. I. & Luna, B. Impact of stress on excitatory and inhibitory markers of
1312 adolescent cognitive critical period plasticity. *Neurosci. Biobehav. Rev.* **153**,
1313 (2023).

1314 81. Yang, X. D. *et al.* Stress during a Critical Postnatal Period Induces Region-
1315 Specific Structural Abnormalities and Dysfunction of the Prefrontal Cortex via
1316 CRF 1. *Neuropsychopharmacology* **40**, 1203–1215 (2015).

1317 82. Dajani, D. R. & Uddin, L. Q. Demystifying cognitive flexibility: Implications for
1318 clinical and developmental neuroscience. *Trends Neurosci.* **38**, 571–578 (2015).

1319 83. Armbruster, D. J. N., Ueltzhöffer, K., Basten, U. & Fiebach, C. J. Prefrontal
1320 cortical mechanisms underlying individual differences in cognitive flexibility and
1321 stability. *J. Cogn. Neurosci.* **24**, 2385–2399 (2012).

1322 84. Gläscher, J. *et al.* Lesion mapping of cognitive control and value-based decision
1323 making in the prefrontal cortex. *Proc. Natl. Acad. Sci. U. S. A.* **109**, 14681–14686
1324 (2012).

1325 85. Durstewitz, D., Vittoz, N. M., Floresco, S. B. & Seamans, J. K. Abrupt transitions
1326 between prefrontal neural ensemble states accompany behavioral transitions
1327 during rule learning. *Neuron* **66**, 438–448 (2010).

1328 86. Milner, B. Effects of Different Brain Lesions on Card Sorting. *Arch Neurol* **9**, 90–
1329 100 (1963).

1330 87. AM, O., Roberts, A., CE, P., BJ, S. & Robbins, T. Extra-dimensional versus intra-
1331 dimensional set shifting performance following frontal lobe excisions, temporal
1332 lobe excisions or amygdalo-hippocampectomy in man. *Neuropsychologia* **29**,
1333 993–1006 (1991).

1334 88. Dias, R., Robbins, T. W. & Roberts, A. C. Dissociable forms of inhibitory control
1335 within prefrontal cortex with an analog of the wisconsin card sort test: Restriction
1336 to novel situations and independence from 'on-line' processing. *J. Neurosci.* **17**,
1337 9285–9297 (1997).

1338 89. Dias, R., Robbins, T. W. & Roberts, A. C. Dissociation in prefrontal cortex of
1339 affective and attentional shifts. *Nature* **380**, 69–72 (1996).

1340 90. Canetta, S. E. *et al.* Mature parvalbumin interneuron function in prefrontal cortex
1341 requires activity during a postnatal sensitive period. *Elife* **11**, 1–24 (2022).

1342 91. Benoit, L. J. *et al.* Adolescent thalamic inhibition leads to long-lasting impairments
1343 in prefrontal cortex function. *Nat. Neurosci.* **25**, 714–725 (2022).

1344 92. Jett, J. D., Bulin, S. E., Hatherall, L. C., McCartney, C. M. & Morilak, D. A. Deficits
1345 in cognitive flexibility induced by chronic unpredictable stress are associated with
1346 impaired glutamate neurotransmission in the rat medial prefrontal cortex.
1347 *Neuroscience* **346**, 284–297 (2017).

1348 93. Birrell, J. M. & Brown, V. J. Medial frontal cortex mediates perceptual attentional
1349 set shifting in the rat. *J. Neurosci.* **20**, 4320–4324 (2000).

1350 94. Brooks, J. M. *et al.* Transient inactivation of the neonatal ventral hippocampus
1351 impairs attentional set-shifting behavior: Reversal with an α7 nicotinic agonist.
1352 *Neuropsychopharmacology* **37**, 2476–2486 (2012).

1353 95. Marquis, J. P., Goulet, S. & Doré, F. Y. Neonatal ventral hippocampus lesions
1354 disrupt extra-dimensional shift and alter dendritic spine density in the medial

1355 prefrontal cortex of juvenile rats. *Neurobiol. Learn. Mem.* **90**, 339–346 (2008).

1356 96. Godsil, B. P., Kiss, J. P., Spedding, M. & Jay, T. M. The hippocampal-prefrontal
1357 pathway: The weak link in psychiatric disorders? *Eur. Neuropsychopharmacol.* **23**,
1358 1165–1181 (2013).

1359 97. Ghoshal, A. & Conn, P. J. The hippocampo-prefrontal pathway: a possible
1360 therapeutic target for negative and cognitive symptoms of schizophrenia. *Futur.*
1361 *Neurol* **10**, 115–128 (2015).

1362 98. Brockmann, M. D., Pöschel, B., Cichon, N. & Hanganu-Opatz, I. L. Coupled
1363 Oscillations Mediate Directed Interactions between Prefrontal Cortex and
1364 Hippocampus of the Neonatal Rat. *Neuron* **71**, 332–347 (2011).

1365 99. Xu, X., Chini, M., Bitzenhofer, S. H. & Hanganu-Opatz, I. L. Transient knock-down
1366 of prefrontal DISC1 in immune-challenged mice causes abnormal long-range
1367 coupling and cognitive dysfunction throughout development. *J. Neurosci.* **39**,
1368 1222–1235 (2019).

1369 100. Caballero, A., Thomases, D. R., Flores-Barrera, E., Cass, D. K. & Tseng, K. Y.
1370 Emergence of GABAergic-dependent regulation of input-specific plasticity in the
1371 adult rat prefrontal cortex during adolescence. *Psychopharmacology (Berl).* **231**,
1372 1789–1796 (2014).

1373 101. Arruda-Carvalho, M., Wu, W. C., Cummings, K. A. & Clem, R. L. Optogenetic
1374 examination of prefrontal-amygdala synaptic development. *J. Neurosci.* **37**, 2976–
1375 2985 (2017).

1376 102. Britt, J. P. *et al.* Synaptic and Behavioral Profile of Multiple Glutamatergic Inputs
1377 to the Nucleus Accumbens. *Neuron* **76**, 790–803 (2012).

1378 103. LeGates, T. A. *et al.* Reward behaviour is regulated by the strength of
1379 hippocampus–nucleus accumbens synapses. *Nature* **564**, 258–262 (2018).

1380 104. Bagot, R. C. *et al.* Ventral hippocampal afferents to the nucleus accumbens
1381 regulate susceptibility to depression. *Nat. Commun.* **6**, (2015).

1382 105. Parfitt, G. M. *et al.* Bidirectional Control of Anxiety-Related Behaviors in Mice:
1383 Role of Inputs Arising from the Ventral Hippocampus to the Lateral Septum and
1384 Medial Prefrontal Cortex. *Neuropsychopharmacology* **42**, 1715–1728 (2017).

1385 106. Glangetas, C. *et al.* NMDA-receptor-dependent plasticity in the bed nucleus of the
1386 stria terminalis triggers long-term anxiolysis. *Nat. Commun.* **8**, (2017).

1387 107. Xu, C. *et al.* Distinct Hippocampal Pathways Mediate Dissociable Roles of
1388 Context in Memory Retrieval. *Cell* **167**, 961-972.e16 (2016).

1389 108. Dolleman-Van Der Weel, M. J. *et al.* The nucleus reuniens of the thalamus sits at

1390 the nexus of a hippocampus and medial prefrontal cortex circuit enabling memory
1391 and behavior. *Learn. Mem.* **26**, 191–205 (2019).

1392 109. Ciocchi, S., Passecker, J., Malagon-Vina, H., Mikus, N. & Klausberger, T.
1393 Selective information routing by ventral hippocampal CA1 projection neurons.
1394 *Science (80-.).* **348**, 560–563 (2015).

1395 110. Padilla-Coreano, N. *et al.* Direct Ventral Hippocampal-Prefrontal Input Is Required
1396 for Anxiety-Related Neural Activity and Behavior. *Neuron* **89**, 857–866 (2016).

1397 111. Adhikari, A., Topiwala, M. A. & Gordon, J. A. Synchronized Activity between the
1398 Ventral Hippocampus and the Medial Prefrontal Cortex during Anxiety. *Neuron*
1399 **65**, 257–269 (2010).

1400 112. Kishi, T., Tsumori, T., Yokota, S. & Yasui, Y. Topographical projection from the
1401 hippocampal formation to the amygdala: A combined anterograde and retrograde
1402 tracing study in the rat. *J. Comp. Neurol.* **496**, 349–368 (2006).

1403 113. Kim, W. Bin & Cho, J. H. Synaptic targeting of double-projecting ventral CA1
1404 hippocampal neurons to the medial prefrontal cortex and basal amygdala. *J.*
1405 *Neurosci.* **37**, 4868–4882 (2017).

1406 114. Hoover, W. B. & Vertes, R. P. Anatomical analysis of afferent projections to the
1407 medial prefrontal cortex in the rat. *Brain Struct. Funct.* **212**, 149–179 (2007).

1408 115. Moser, M. & Moser, E. I. Distributed Encoding and Retrieval of Spatial Memory in
1409 the Hippocampus. **18**, 7535–7542 (1998).

1410 116. Dong, H. W. & Swanson, L. W. Projections from bed nuclei of the stria terminalis,
1411 anteromedial area: Cerebral hemisphere integration of neuroendocrine,
1412 autonomic, and behavioral aspects of energy balance. *J. Comp. Neurol.* **494**,
1413 142–178 (2006).

1414 117. Rizzi-Wise, C. A. & Wang, D. V. Putting together pieces of the lateral septum:
1415 Multifaceted functions and its neural pathways. *eNeuro* **8**, (2021).

1416 118. Churchwell, J. C., Morris, A. M., Musso, N. D. & Kesner, R. P. Prefrontal and
1417 hippocampal contributions to encoding and retrieval of spatial memory. *Neurobiol.*
1418 *Learn. Mem.* **93**, 415–421 (2010).

1419 119. Morici, J. F., Weisstaub, N. V. & Zold, C. L. Hippocampal-medial prefrontal cortex
1420 network dynamics predict performance during retrieval in a context-guided object
1421 memory task. *Proc. Natl. Acad. Sci. U. S. A.* **119**, 1–12 (2022).

1422 120. Sierra-Mercado, D., Padilla-Coreano, N. & Quirk, G. J. Dissociable roles of
1423 prelimbic and infralimbic cortices, ventral hippocampus, and basolateral amygdala
1424 in the expression and extinction of conditioned fear. *Neuropsychopharmacology*
1425 **36**, 529–538 (2011).

1426 121. Wang, N. *et al.* Role of Glutamatergic Projections from the Ventral CA1 to
1427 Infralimbic Cortex in Context-Induced Reinstatement of Heroin Seeking.
1428 *Neuropsychopharmacology* **43**, 1373–1384 (2018).

1429 122. Brockway, E. T., Simon, S. & Drew, M. R. Ventral hippocampal projections to
1430 infralimbic cortex and basolateral amygdala are differentially activated by
1431 contextual fear and extinction recall. *Neurobiol. Learn. Mem.* **205**, 107832 (2023).

1432 123. Spear, L. P. *The adolescent brain and age-related behavioral manifestations.*
1433 *Neuroscience and biobehavioral reviews* vol. 24 (2000).

1434 124. Reincke, S. A. J. & Hanganu-opatz, I. L. Early-life stress impairs recognition
1435 memory and perturbs the functional maturation of prefrontal- hippocampal-
1436 perirhinal networks. *Sci. Rep.* 1–16 (2017) doi:10.1038/srep42042.

1437 125. Wang, H. X. & Gao, W. J. Cell type-specific development of NMDA receptors in
1438 the interneurons of rat prefrontal cortex. *Neuropsychopharmacology* **34**, 2028–
1439 2040 (2009).

1440 126. Kirkwood, A., Lee, H. & Bear, M. Co-regulation of long-term potentiation and
1441 experience-dependent synaptic plasticity in visual cortex by age and experience.
1442 *Nature* **375**, 328–31 (1995).

1443 127. Antonini, a, Fagiolini, M. & Stryker, M. P. Anatomical correlates of functional
1444 plasticity in mouse visual cortex. *J. Neurosci.* **19**, 4388–406 (1999).

1445 128. Antonini, A. & Stryker, M. P. Rapid Remodeling of Axonal Arbors in the Visual
1446 Cortex. *Science (80-.).* **260**, 1819–1821 (1993).

1447 129. Holtmaat, A. J. G. D. *et al.* Transient and persistent dendritic spines in the
1448 neocortex in vivo. *Neuron* **45**, 279–291 (2005).

1449 130. Zuo, Y., Lin, A., Chang, P. & Gan, W. B. Development of long-term dendritic spine
1450 stability in diverse regions of cerebral cortex. *Neuron* **46**, 181–189 (2005).

1451 131. Botterill, J. J., Gerencer, K. J., Vinod, K. Y., Alcantara-Gonzalez, D. & Scharfman,
1452 H. E. Dorsal and ventral mossy cells differ in their axonal projections throughout
1453 the dentate gyrus of the mouse hippocampus. *Hippocampus* **31**, 522–539 (2021).

1454 132. Botterill, J. J. *et al.* Dorsal peduncular cortex activity modulates affective behavior
1455 and fear extinction in mice. *Neuropsychopharmacology* 1–14 (2024)
1456 doi:10.1038/s41386-024-01795-5.

1457 133. Linke, R., Pabst, T. & Frotscher, M. Development of the hippocamposeptal
1458 projection in the rat. *J. Comp. Neurol.* **351**, 602–616 (1995).

1459 134. Tsamis, K. I., Lagartos Donato, M. J., Dahl, A. G., O'Reilly, K. C. & Witter, M. P.
1460 Development and topographic organization of subicular projections to lateral

1461 septum in the rat brain. *Eur. J. Neurosci.* **52**, 3140–3159 (2020).

1462 135. Zhang, Z. W. Maturation of Layer V Pyramidal Neurons in the Rat Prefrontal
1463 Cortex: Intrinsic Properties and Synaptic Function. *J. Neurophysiol.* **91**, 1171–
1464 1182 (2004).

1465 136. Kroon, T., van Hugte, E., van Linge, L., Mansvelder, H. D. & Meredith, R. M. Early
1466 postnatal development of pyramidal neurons across layers of the mouse medial
1467 prefrontal cortex. *Sci. Rep.* **9**, (2019).

1468 137. Van Eden, C. G., Kros, J. M. & Uylings, H. B. M. Chapter 8 The development of
1469 the rat prefrontal cortex: Its size and development of connections with thalamus,
1470 spinal cord and other cortical areas. *Prog. Brain Res.* **85**, 169–183 (1991).

1471 138. Reynolds, L. M. & Flores, C. Mesocorticolimbic Dopamine Pathways Across
1472 Adolescence: Diversity in Development. *Front. Neural Circuits* **15**, 1–17 (2021).

1473 139. Reynolds, L. M. *et al.* DCC Receptors Drive Prefrontal Cortex Maturation by
1474 Determining Dopamine Axon Targeting in Adolescence. *Biol. Psychiatry* 1–12
1475 (2017) doi:10.1016/j.biopsych.2017.06.009.

1476 140. Hoops, D., Reynolds, L. M. & Flores, C. Dopamine Development in the Mouse
1477 Orbital Prefrontal Cortex Is Protracted and Sensitive to Amphetamine in
1478 Adolescence. **5**, 1–9 (2018).

1479 141. Reynolds, L. M. *et al.* Early Adolescence is a Critical Period for the Maturation of
1480 Inhibitory Behavior. *Cereb. Cortex* **29**, 3676–3686 (2019).

1481 142. Gergues, M. M. *et al.* Circuit and molecular architecture of a ventral hippocampal
1482 network. *Nat. Neurosci.* **23**, 1444–1452 (2020).

1483 143. Ueda, S. *et al.* Sequence of Molecular Events during the Maturation of the
1484 Developing Mouse Prefrontal Cortex. *Mol. Neuropsychiatry* **1**, 94–104 (2015).

1485 144. Miyamae, T., Chen, K., Lewis, D. A. & Gonzalez-Burgos, G. Distinct physiological
1486 maturation of parvalbumin-positive neuron subtypes in mouse prefrontal cortex. *J.*
1487 *Neurosci.* **37**, 4883–4902 (2017).

1488 145. Yang, J. M., Zhang, J., Yu, Y. Q., Duan, S. & Li, X. M. Postnatal development of 2
1489 microcircuits involving fast-spiking interneurons in the mouse prefrontal cortex.
1490 *Cereb. Cortex* **24**, 98–109 (2014).

1491 146. Canetta, S. *et al.* Mature parvalbumin interneuron function in prefrontal cortex
1492 requires activity during a postnatal sensitive period. *bioRxiv* 7031–7031 (2022)
1493 doi:10.1007/978-3-319-19650-3_304535.

1494 147. Song, L. *et al.* Sparser and Less Efficient Hippocampal-Prefrontal Projections
1495 account for Developmental Network Dysfunction in a Model of Psychiatric Risk

1496 Mediated by Gene-Environment Interaction. *J. Neurosci.* **42**, 601–618 (2022).

1497 148. Parent, M. A., Wang, L., Su, J., Netoff, T. & Yuan, L. L. Identification of the
1498 hippocampal input to medial prefrontal cortex in vitro. *Cereb. Cortex* **20**, 393–403
1499 (2010).

1500 149. Jay, T. M., Glowinski, J. & Thierry, A. M. Selectivity of the hippocampal projection
1501 to the prelimbic area of the prefrontal cortex in the rat. *Brain Res.* **505**, 337–340
1502 (1989).

1503 150. Liu, X., Dimidschstein, J., Fishell, G. & Carter, A. G. Hippocampal inputs engage
1504 cck+ interneurons to mediate endocannabinoid-modulated feed-forward inhibition
1505 in the prefrontal cortex. *Elife* **9**, 1–22 (2020).

1506 151. Zhang, Z. Maturation of Layer V Pyramidal Neurons in the Rat Prefrontal Cortex :
1507 Intrinsic Properties and Synaptic Function. *J. Neurophysiol.* **91**, 1171–1182
1508 (2004).

1509 152. Cizeron, M. *et al.* A brainwide atlas of synapses across the mouse life span.
1510 *Science (80-.).* **369**, 270–275 (2020).

1511 153. Bolles, R. C. & Woods, P. J. The ontogeny of behaviour in the albino rat. *Anim.*
1512 *Behav.* **12**, 427–441 (1964).

1513 154. Akers, K. G., Arruda-Carvalho, M., Josselyn, S. A. & Frankland, P. W. Ontogeny
1514 of contextual fear memory formation, specificity, and persistence in mice. *Learn.*
1515 *Mem.* **19**, 598–604 (2012).

1516 155. Josselyn, S. a. & Frankland, P. W. Infantile amnesia: A neurogenic hypothesis.
1517 *Learn. Mem.* **19**, 423–433 (2012).

1518 156. Guskjolen, A. *et al.* Recovery of “Lost” Infant Memories in Mice. *Curr. Biol.* **28**,
1519 2283-2290.e3 (2018).

1520 157. Guskjolen, A., Josselyn, S. A. & Frankland, P. W. Age-dependent changes in
1521 spatial memory retention and flexibility in mice. *Neurobiol. Learn. Mem.* **143**, 59–
1522 66 (2017).

1523 158. Samifanni, R. *et al.* Developmental emergence of persistent memory for
1524 contextual and auditory fear in mice. *Learn Mem* **28**, 414–421 (2021).

1525 159. Li, S., Kim, J. H. & Richardson, R. Updating memories: Changing the involvement
1526 of the prelimbic cortex in the expression of an infant fear memory. *Neuroscience*
1527 **222**, 316–325 (2012).

1528 160. Sellinger, E. P., Drzewiecki, C. M., Willing, J. & Juraska, J. M. Cell death in the
1529 male and female rat medial prefrontal cortex during early postnatal development.
1530 *IBRO Neurosci. Reports* **10**, 186–190 (2021).

1531 161. Premachandran, H., Zhao, M. & Arruda-Carvalho, M. Sex Differences in the
1532 Development of the Rodent Corticolimbic System. *Front. Neurosci.* **14**, (2020).

1533 162. Brenhouse, H. C. & Andersen, S. L. Developmental trajectories during
1534 adolescence in males and females: A cross-species understanding of underlying
1535 brain changes. *Neurosci. Biobehav. Rev.* **35**, 1687–1703 (2011).

1536 163. Walker, D. M. *et al.* Adolescence and reward: Making sense of neural and
1537 behavioral changes amid the chaos. *J. Neurosci.* **37**, 10855–10866 (2017).

1538 164. Koss, W. A., Belden, C. E., Hristov, A. D. & Juraska, J. M. Dendritic remodeling in
1539 the adolescent medial prefrontal cortex and the basolateral amygdala of male and
1540 female rats. *Synapse* **68**, 61–72 (2014).

1541 165. Derks, N. A. V., Krugers, H. J., Hoogenraad, C. C., Joëls, M. & Angela
1542 Sarabdjitsingh, R. Effects of early life stress on synaptic plasticity in the
1543 developing hippocampus of male and female rats. *PLoS One* **11**, 1–17 (2016).

1544 166. Zitman, F. M. & Richter-Levin, G. Age and sex-dependent differences in activity,
1545 plasticity and response to stress in the dentate gyrus. *Neuroscience* **249**, 21–30
1546 (2013).

1547 167. Rabiant, K., Antol, J., Naassila, M. & Pierrefiche, O. Sex difference in the
1548 vulnerability to hippocampus plasticity impairment after binge-like ethanol
1549 exposure in adolescent rat: Is estrogen the key? *Addict. Biol.* **26**, 1–12 (2021).

1550 168. Page, C. E. & Coutellier, L. Adolescent Stress Disrupts the Maturation of Anxiety-
1551 related Behaviors and Alters the Developmental Trajectory of the Prefrontal
1552 Cortex in a Sex- and Age-specific Manner. *Neuroscience* **390**, 265–277 (2018).

1553 169. Bueno-Fernandez, C. *et al.* Long term effects of peripubertal stress on excitatory
1554 and inhibitory circuits in the prefrontal cortex of male and female mice. *Neurobiol.*
1555 *Stress* **14**, (2021).

1556 170. Urban, K. R. & Valentino, R. J. Age- And sex-dependent impact of repeated social
1557 stress on intrinsic and synaptic excitability of the rat prefrontal cortex. *Cereb.*
1558 *Cortex* **27**, 244–253 (2017).

1559 171. Wei, J. *et al.* Estrogen protects against the detrimental effects of repeated stress
1560 on glutamatergic transmission and cognition. *Mol. Psychiatry* **19**, 588–598 (2014).

1561 172. Muir, J. *et al.* Sex-biased neural encoding of threat discrimination in nucleus
1562 accumbens afferents drives suppression of reward behavior. *Nat. Neurosci.*
1563 (2024) doi:10.1038/s41593-024-01748-7.

1564 173. Gruene, T. M., Roberts, E., Thomas, V., Ronzio, A. & Shansky, R. M. Sex-specific
1565 neuroanatomical correlates of fear expression in prefrontal-amygdala circuits.
1566 *Biol. Psychiatry* **78**, 186–193 (2015).

174. Lay, B., Esber, G. & Iordanova, M. D. Reduction in reward-driven behaviour depends on the basolateral but not central nucleus of the amygdala in female rats. *J. Neurosci.* (2025).

175. Dulac, C. & Kimchi, T. Neural mechanisms underlying sex-specific behaviors in vertebrates. *Curr. Opin. Neurobiol.* **17**, 675–683 (2007).

176. Juraska, J. M. & Willing, J. Pubertal onset as a critical transition for neural development and cognition. *Brain Res.* **1654**, 87–94 (2017).

177. Willing, J., Drzewiecki, C. M., Cuenod, B. A., Cortes, L. R. & Juraska, J. M. A role for puberty in water maze performance in male and female rats. *Behav. Neurosci.* **130**, 422–427 (2016).

178. Piekarski, D. J., Boivin, J. R. & Wilbrecht, L. Ovarian Hormones Organize the Maturation of Inhibitory Neurotransmission in the Frontal Cortex at Puberty Onset in Female Mice. *Curr. Biol.* **27**, 1735-1745.e3 (2017).

179. Piekarski, D. J. *et al.* Does puberty mark a transition in sensitive periods for plasticity in the associative neocortex? *Brain Res.* **1654**, 123–144 (2017).

180. Griffiths, B. B., Madden, A. M. K., Edwards, K. A., Zup, S. L. & Stary, C. M. Age-dependent sexual dimorphism in hippocampal cornu ammonis-1 perineuronal net expression in rats. *Brain Behav.* **9**, 1–5 (2019).

181. Drzewiecki, C. M., Willing, J. & Juraska, J. M. Influences of age and pubertal status on number and intensity of perineuronal nets in the rat medial prefrontal cortex. *Brain Struct. Funct.* **225**, 2495–2507 (2020).

182. Hensch, T. K. Critical Period Mechanisms in Developing Visual Cortex. *Curr. Top. Dev. Biol.* **69**, 215–237 (2005).

183. Hensch, T. K. Local GABA Circuit Control of Experience-Dependent Plasticity in Developing Visual Cortex. *Science (80-.).* **282**, 1504–1508 (1998).

184. Iwai, Y., Fagiolini, M., Obata, K. & Hensch, T. K. Rapid critical period induction by tonic inhibition in visual cortex. *J. Neurosci.* **23**, 6695–6702 (2003).

185. Premachandran, H., Wilkin, J. & Arruda-carvalho, M. Minimizing Variability in Developmental Fear Studies in Mice : Toward Improved Replicability in The Field. 1–25 (2024) doi:10.1002/cpz1.1040.

186. Canetta, S. *et al.* Differential Synaptic Dynamics and Circuit Connectivity of Hippocampal and Thalamic Inputs to the Prefrontal Cortex. *Cereb. Cortex Commun.* **1**, 1–15 (2020).

187. Pöpplau, J. A. *et al.* Reorganization of adolescent prefrontal cortex circuitry is required for mouse cognitive maturation. *Neuron* **112**, 421-440.e7 (2024).

188. Reynolds, L. M. *et al.* Amphetamine disrupts dopamine axon growth in adolescence by a sex-specific mechanism in mice. *Nat. Commun.* **14**, (2023).

189. Bitzenhofer, S. H., Pöpplau, J. A., Chini, M., Marquardt, A. & Hanganu-Opatz, I. L. A transient developmental increase in prefrontal activity alters network maturation and causes cognitive dysfunction in adult mice. *Neuron* **109**, 1350-1364.e6 (2021).

190. Morgan, A. A. *et al.* Medial Prefrontal Cortex Serotonin Input Regulates Cognitive Flexibility in Mice. *bioRxiv Prepr. Serv. Biol.* **6216**, 1–34 (2023).

191. Spear, L. The adolescent brain and age-related behavioral manifestations. *Neurosci. Biobehav. Rev.* **24**, 417–463 (2000).

192. Cruz-Sanchez, A. *et al.* Developmental onset distinguishes three types of spontaneous recognition memory in mice. *Sci. Rep.* **10**, 25–26 (2020).

193. Franklin, K. B. J. & Paxinos, G. *The Mouse Brain in Stereotaxic Coordinates (map)*. *Academic Press* (2007).

194. Arruda-Carvalho, M. & Clem, R. L. Pathway-selective adjustment of prefrontal-amygdala transmission during fear encoding. *J. Neurosci.* **34**, 15601–15609 (2014).

195. Cruikshank, S. J., Urabe, H., Nurmikko, A. V. & Connors, B. W. Pathway-Specific Feedforward Circuits between Thalamus and Neocortex Revealed by Selective Optical Stimulation of Axons. *Neuron* **65**, 230–245 (2010).